

# Thermal model for analysis of Mars infrared mapping

Hugh H. Kieffer<sup>1,2</sup>

Received 20 June 2012; revised 13 November 2012; accepted 20 November 2012; published 29 March 2013.

[1] The KRC numerical thermal model has been used in the analysis of observations from virtually all Mars missions with infrared sensors and for the selection of virtually all Mars' landing sites. It uses a physics-based one-layer atmosphere gray at solar and thermal wavelengths to determine the radiative effect of a dusty atmosphere. One gas component may condense to form a seasonal polar cap and affect the global surface pressure. The atmosphere may be omitted entirely to model airless bodies. KRC uses layers that become thicker geometrically with depth and it uses repeated time step doubling. The surface may be homogeneous or have two zones of material properties, each zone may have temperature-dependent thermal conductivity and specific heat. Surface slopes or depressions are modeled to first order. Here KRC is described in detail and used to compute globally the annual average surface temperature accounting for albedo, thermal inertia, elevation, slope at 3 km resolution, and zonal climate. Comparisons with three other thermal models are discussed. The model is available for general use.

**Citation:** Kieffer, H. H. (2013), Thermal model for analysis of Mars infrared mapping, *J. Geophys. Res. Planets*, 118, 451–470, doi:10.1029/2012JE004164.

## 1. Introduction

[2] This paper describes a numerical model used extensively for computing planetary surface temperatures. The KRC numerical model has evolved over a period of five decades and has been used for a variety of planet, satellite, and comet problems; however, use has concentrated on Mars. The model uses a one-layer atmosphere but does allow condensation and global pressure variation; the model can output surface kinetic and planetary (nadir view from space) bolometric temperatures, along with a variety of parameters related to subsurface-layer and atmosphere temperatures, seasonal polar cap mass, heat-flow and numerical performance parameters.

[3] The program is designed to compute surface and subsurface temperatures for a global set of latitudes at a full set of seasons, with enough depth to capture the annual thermal wave and to compute seasonal condensation mass. For historic reasons (it originated in the era of kilohertz processors), the code has substantial optimization. It allows sloped surfaces and two zones of different subsurface materials. There are generalities that allow this code set to be used for any ellipsoid with any spin vector, in any orbit (around any star),

with or without an atmosphere (including condensation); this is also the source of some of the complexity.

[4] In response to an oft-asked question, the acronym KRC is simply *K* for conductivity, *R* for “rho” ( $\rho$ ) for density, and *C* for specific heat—the three terms in thermal inertia *I*. KRC uses explicit forward finite differences and is coded in FORTRAN (with some utility C routines). Model development began in 1968, and was used to support the Viking mission with a total of three cases in an era when computing a single case for 19 latitudes at 40 seasons with a 2 year spin-up took an hour on a large university unshared mainframe computer. For this reason, the code is highly optimized for speed and uses layer thickness increasing exponentially downward and time steps that increase by factors of two deeper into the subsurface where stability criteria are met. The code is modularized based on time scale and function, and there is extensive use of Commons. The version used for Mariner 9 and Viking was described briefly in Kieffer *et al.* [1977]. The KRC model was used in many analyses of the Viking Infrared Thermal Mapper (IRTM) data; derivatives were used to study sublimating comets [Weissman and Kieffer, 1981] and ring and satellite eclipses [Aumann and Kieffer, 1973; Gatley *et al.*, 1974; Lunine *et al.*, 1982]. The code has undergone stepwise revision, a major change being a 2002 replacement of a down-going steady IR flux equivalent to fixed fraction of the noon insolation with the atmosphere described here. This newer version has been the basis for analysis of Thermal Emission Imaging System (THEMIS) and Mars Exploration Rover (MER) Mini-TES results. As of 2009, the code allows temperature-dependent thermal conductivity and specific-heat.

[5] Although KRC has many loops to compute temperatures as a function of time-of-day, latitude, season, and a multitude of physical parameters, a key characteristic is that

All Supporting Information may be found in the online version of this article.

<sup>1</sup>Celestial Reasonings, Genoa, Nevada, USA.

<sup>2</sup>Space Science Institute, Boulder, Colorado, USA.

Corresponding author: H. H. Kieffer, Celestial Reasonings, 180 Snowshoe Ln., POB 1057, Genoa, NV 89411-1057, USA. (hkierfer@charter.net)

©2012. American Geophysical Union. All Rights Reserved. 2169-9097/13/2012JE004164

at its core it only computes one surface temperature at a time. A number of first-order approximations are used to accommodate slopes and circular depressions without an appreciable decrease in speed.

[6] For THEMIS, a “one-point” (OnePoint) capability was included that allows input of a set of points defined by season, latitude, hour, and a few major physical parameters; KRC will produce the surface kinetic temperature and planetary brightness temperature for these points (see section 5.6).

[7] The data sets that constitute the online Supporting Information include all source code, guides for installation and running KRC, supporting documentation, sample input and output files. The full source code and documentation will be maintained and available at the KRC website: <http://krc.mars.asu.edu>.

### 1.1. Use for Recent Missions

[8] Determination of thermal inertia using the KRC model has been used in selecting all landing sites on Mars: Viking [Ezell and Ezell, 1984, p.352+]; Pathfinder [Golombek et al., 1997a]; MER [Christensen et al., 2005a; Golombek et al., 2003]; Phoenix [Arvidson et al., 2008]; Mars Science Laboratory (MSL) [Ferguson et al., 2012; Golombek et al., 2012]. Rock abundances have been computed using the KRC model [Christensen, 1986] and postlanding assessment has shown the estimates based on IR observations to be close [Golombek et al., 1997b, 2005; Nowicki and Christensen, 2007].

[9] Standard data reduction of the Odyssey THEMIS uses the KRC model [Christensen et al., 2003, 2005b; Rogers et al., 2005; Titus et al., 2003]. This involved generation of a large set of models on a grid of thermal inertia  $I$ , surface albedo  $A$ , elevations and visual dust opacities  $\tau_0$  with output of surface kinetic temperature  $T_s$ , and top-of-atmosphere bolometric temperature  $T_b$  at a uniform set of latitudes, hours (h, 1/24 of the planets day), and seasons. The seven-dimensional model set is interpolated first in season (to correspond to a specific Odyssey orbit), then at the latitude and hour of each observation using the elevation corresponding to the observation longitude; interpolation in opacity and albedo are based on prior or current observations. This leaves  $T_s$  and  $T_b$  as a function of thermal inertia, which may not be monotonic; this relation is interpolated linearly in  $T$ , using either  $T_b$  or opacity-corrected  $T_s$ , and logarithmically in  $I$  to get the thermal inertia. KRC was used in analysis and surface thermal observations by Mini-TES, usually with a similar scheme for  $T_s$  only [Golombek et al., 2006; Ferguson et al., 2006a].

[10] KRC thermal modeling has been used for the study of the general nature of the Martian surface [Bandfield, 2007; Bandfield and Edwards, 2008; Bandfield and Feldman, 2008; Edgett and Christensen, 1991; Arvidson et al., 2006; Bell, 2008]; and detailed sites [Arvidson et al., 2004; Christensen et al., 2004; Feldman et al., 2008; Ferguson et al., 2006a, 2006b; Glotch and Christensen, 2005; Greeley et al., 2006; Ruff et al., 2001].

[11] KRC has been used in many analyses of Thermal Emission Spectrometer (TES) data [e.g., Nowicki and Christensen, 2007; Osterloo et al., 2008].

[12] KRC models are the basis for the surface temperature estimate used for the black-body emission correction to

Mars Reconnaissance Orbiter Compact Reconnaissance Imaging Spectrometer for Mars reflection spectra [Martin, 2004].

[13] KRC [Kieffer, 2007] and derivatives [Piqueux and Christensen, 2008; Piqueux et al., 2008] have been used in the study of seasonal slab ice. The capability to model temperatures at the bottom of conical depressions was added to study the potential volatile sublimation in freshly exposed trenches to be dug by the Phoenix mission; this geometric capability can as well be applied to the floors of craters.

[14] In an extreme case, a movie of a thermal day on Mars was made by computing surface temperatures at 0.017 h intervals with a “spin-up” of 5 sols at  $L_s = 90^\circ$ . The measured albedo, thermal inertia, and elevation with  $0.25^\circ$  resolution in longitude and latitude was used. 1.45 billion instances of KRC OnePoint mode were run on a cluster of 128 CPUs for 48 h over a weekend. The video can be viewed at [http://mars.asu.edu/phil/ls90\\_32\\_full\\_5\\_part\\_movie.mov](http://mars.asu.edu/phil/ls90_32_full_5_part_movie.mov) (P. Christensen, personal communication). A version of KRC specifically modified later for this application increased the speed by a factor of 3800.

### 1.2. Some Other Thermal Models Used for Mars

[15] The Martian atmosphere has a significant effect on surface temperature, both in the physical temperature of the surface being influenced by the dusty atmosphere’s modification of the insolation that reaches the surface and the down-going infrared radiation from the atmosphere, and on the apparent temperature measured remotely by infrared radiometry [Haberle and Jakosky, 1991]. Thermal models that treat the atmosphere in detail, such as a dusty radiative/convective column [Haberle and Jakosky, 1991] or that include lateral heat transport such in a General Circulation Model (GCM) [Haberle et al., 1993; Barnes et al., 1993], generally take two to several orders of magnitude longer than KRC to run.

[16] The thermal models for the Mars Global Surveyor (MGS) TES standard data processing were based on the Mellon-Jakosky-Haberle model (hereafter simply the Mellon model) [Jakosky et al., 2000; Mellon et al., 2000]. The Mellon model has direct heritage from KRC and uses a similar subsurface; it has a multilayer conductive/convective atmosphere with radiative properties based on calculations by Jim Pollack whose basis has been lost (community oral history). Extensive comparison of the Mellon model and KRC was done in the development of the MGS TES production code (see section 3.4.3). This model has been used in detailed global mapping of TES observations [Putzig et al., 2005].

[17] Schorghofer and Aharonson developed a model in which treatment of the atmosphere and slopes is based on KRC. This model uses the Crank-Nicolson scheme and includes vapor diffusion in the soil; it has been used to study the distribution of ice in current and prior climates [Schorghofer and Aharonson, 2005; Aharonson and Schorghofer, 2006; Schorghofer, 2008]. Helbert and Benkhoff developed a model that allows detailed layering of properties and vapor diffusion [Helbert and Benkhoff, 2003].

[18] A finite-difference thermal model used for estimating depth to liquid water stability [Clifford and Bartels, 1986]

**Table 1.** Symbols and Variables<sup>a</sup>

Symbol	Name in Code	Input File Label or Equation	Value + Frequency	Description and Basis
$A$	AS	ALBEDO	$S, R_f$	Current bolometric albedo.
$B_i$	B		O	Thickness of layer $i$ [m].
$C$	SPHT	SpecHeat, SpHeat2	C	Specific heat of solid material
$c_p$	ATMCP	Atm_Cp	860. C	Atm. specific heat at constant pressure. $\text{J K}^{-1} \text{kg}^{-1}$ , MARS p.855
$C_1$	CABR	CABR	0.11 C	Clear atmosphere IR absorption for PTOTAL column
$C_2$	TAURAT	TAURAT	0.5 C	Dust IR/vis relative opacity. MARS p.1022,1025
$F_3$	FAC3	$(1 - A_{\text{IR}})$	$S, R_f$	Surface solar absorbance.
$F_4$	FAC4	$1 + 1/RLAY$	O	Layer factor.
$F_5$	FAC5	$\Omega \epsilon \sigma$	O	Surface thermal emission factor.
$4F_5$	FAC45	$4\Omega \epsilon \sigma$	O	Surface thermal emission factor
$F_6$	FAC6	$\Omega \epsilon_{\text{[f]}}$	O	Surface emission factor.
$F_7$	FAC7	$\frac{k}{X_2}$	O	Layer scaling.
$F_8$	FAC8	$e^{-\tau_R} \epsilon_{\text{[f]}}$	O	Fraction of surface blackbody reaching top-of-atmosphere.
$F_9$	FAC9	$\sigma(1 - e^{-\tau_e})$	O	Fractional atmospheric radiation
$g$	GRAV	GRAV	3.727 C	Martian gravity. $\text{m s}^{-2}$
$G_H$	GO	ARC2	0.5 C	Henyey-Greenstein asymmetry. MARS p.1030
$\mathcal{H}$	SCALEH		S	Scale height in km.
$H$		$-k \frac{dT}{dz}$		Heat flow
$H_V$	ADGR	S	SR	Solar heating of atm. $\text{W m}^{-2}$
$i$	I, J			Layer index, increasing downward.
$i_0$			SR	Incidence angle from zenith onto a horizontal surface.
$i_2$			SR	Incidence angle onto local slope; from SLOPE and SLOAZI
$I$	SKRC	INERTIA		Thermal inertia $\equiv \sqrt{k\rho c}$ , $\text{J m}^{-2} \text{s}^{-1/2} \text{K}^{-1}$
$k$	COND	COND	C	Thermal conductivity of the soil. $\text{W m}^{-1} \text{K}^{-1}$
$M$			$R_f$	Columnar mass of $\text{CO}_2$ frost $\text{kg m}^{-2}$
$\mathcal{M}$	AMW		43.5 C	Atomic weight of general atmosphere. (g/mole).
$P$	PERSEC	PERIOD [days]	C	Diurnal period in seconds
$P_0$	PTOTAL	PTOTAL	540. C	Mean annual total pressure at elevation =0. if KPREF is 0 or 1. Pa If KPREF is 2, then it is the global atm. plus seasonal cap inventory.
$P_g$	PZREF		S	Current pressure at reference level. Pa
$P$	PRES		S	Current local surface pressure. Pa
$R$	RLAY	RLAY	C	Ratio of thickness of succeeding layers
$R_{\text{vis}}$	ATMRAD	$F_9 T_a^4$	R	Hemispheric emission from a gray slab atmosphere. $\text{W m}^{-2}$
$S_0$	SOLCON	SOLCON	1368. C	Solar constant. $\text{W m}^{-2}$
$S_M$	SOL	$S_0/U^2$	S	Solar flux at Mars. $\text{W m}^{-2}$
$S'_{(i)}$	ASOL		SR	Total insolation onto [sloped] surface. $\text{W m}^{-2}$

<sup>a</sup>Computation frequency (for the temperature-independent properties case) is indicated as: C=Input constant; F=Firm-coded constant; O=Once; S=Every “season” of latitude (may be as frequent as each sol); H=Every “Hour” (24 times per sol); R=Rapid: every time step (nominal is 384 times per sol); SR=every time step for one day each season; subscript [f] means that frost values are used if frost is present; ‘MARS’ indicates that the values were taken from Kieffer *et al.* [1992] at the listed page.

was made publicly available. A derivative of this model and KRC was used to study ground ice stability [Paige, 1992].

[19] A model similar to KRC in subsurface representation was used largely for Mars’ polar studies [Paige and Wood, 1992; Wood and Paige, 1992; Paige *et al.*, 1994; Paige and Keegan, 1994].

### 1.3. Notation Use Here

[20] Program and routine names are shown as **PROGRM**. Code variable names are shown **VARIAB**. Input parameters are shown as **INPUT**. File names are shown as *file*.

[21] For convenience, some physical parameter default values are shown within square brackets at their point of mention and some are listed in Table 1, which contain symbols, variable names, and some indication of how often various terms are calculated.

[22] All units are SI, except the use of days [86,400 s] for orbital motion. The sample input file, Dataset 8, includes all input parameters. The symbols  $T_s$  and  $T_a$  are used in the text

for kinetic temperature of the surface and the one-layer atmosphere.

## 2. Physical Representation

[23] KRC solves the heat diffusion equation (equation (15)) with an upper boundary condition (equation (13)) that includes periodic insolation through a dusty (and cloudy) atmosphere, infrared radiative transfer with the atmosphere, and condensation and accumulation of diurnal and seasonal frosts. The primary outputs are kinetic surface temperature  $T_s$  and bolometric “top-of-the-atmosphere” temperature  $T_b$  as might be measured by a remote observer, both as functions of “hour” (local time of day), season, and latitude; it can also produce subsurface layer temperatures, atmosphere temperature, and frost amounts.

[24] KRC is designed to do this for a spinning ellipsoid (e.g., Mars) in an elliptical orbit for periods of a few “sols” (body rotation periods) to many “years” (orbital periods). All the planetary (or satellite or asteroid) values

**Table 1.** (continued) Symbols and Variables

Symbol	Name in Code	Input File Label or Equation	Value + Frequency	Description and Basis
$t$			-	Time; through a sol from midnight.
$\Delta t$	DTIM			Smallest time step
$T$	TSUR		R	Surface kinetic temperature. Kelvin
$T_a$	TATM, TATMJ	TATM	200. C,R	Temperature of the atmosphere. Kelvin
$T_b$	TPFH		R	Nadir top-of-atmosphere bolometric temperature. Kelvin
$T_s$	TSUR		R	Surface kinetic temperature. Kelvin
$U$	DAU	DAU	S	Heliocentric range. Astronomical Units
$W$	POWER		R	Energy into the surface boundary. $\text{W m}^{-2}$
$X$	XCEN	XCEN	O	Depth to middle of each layer [m]
$\alpha$	1-SKYFAC	$\alpha$	S	Fraction of upper hemisphere occupied by ground
$\beta$	BETA	$1 - e^{-\tau_R}$	S	Vertical thermal absorption of atmosphere
$\beta_e$	BETH	$1 - e^{-\tau_e}$	S	Hemispheric thermal absorption of atmosphere
$\gamma$	TWILFAC		S	Twilight extension factor
$\delta$	[ R] SDEC	SOLARDEC	S	Sub-solar latitude degree [ $R$ =radian].
$\epsilon_{[f]}$	EMIS	EMIS	S,R <sub>f</sub>	Surface emissivity. FEMIS for frost
$\theta$	DLAT		S	Latitude. $\theta_2$ = latitude + slope north
$\kappa$	DIFFI	$\frac{k}{\rho C}$	O	Thermal diffusivity, $\text{m}^2 \text{s}^{-1}$
$\mu_0$	COSI	$\cos i$	SR	Cosine of the incidence angle
$\varpi$	OMEGA	DUSTA	0.9 C	Dust grain single scattering albedo. MARS p.1030
$\rho$	DENS	DENSITY,DENS2	C	bulk density
$\sigma$	SIGSB	5.67051e-8	F	Stephan-Boltzmann constant. $\text{W m}^{-2} \text{K}^{-4}$
$\tau$				generic opacity
$\tau_0$	TAUD	TAUD	0.2 C	Solar-wavelengths dust opacity at $P_0$
$\tau_i$	TAUICE		S	Infrared opacity of ice aerosols
$\tau_e$	TAUEFF	Equation (4)	S	Effective thermal opacity of the atmosphere
$\tau_R$	TAUIR		S	Total thermal opacity, zenith
$\tau_v$	OPACITY		S	Current local total visual opacity
$\phi$	ANGLE		R	Hour angle from midnight, $\phi_2$ = hour angle + slope east
$\Omega$	SKYFAC	$\equiv 1 - \alpha$	SR	Fraction of the upper hemisphere that is sky
$\langle \rangle$				diurnally-averaged value
	TWILI	TWILI	1.0 C	Central angle extension of twilight, degrees
	DTAFAC	$\Delta t / \left( c_p \frac{P}{g} \right)$	O	Atmosphere heating factor. $\text{s}^2 \text{m}^2 \text{K W}^{-1}$
	FEMIT	$\Omega \epsilon_f \sigma T_f^4$	O	Frost thermal emission. $\text{W m}^{-2}$

are specified by a set of about 100 input parameters, described in the Datasets 7 and 8; some are in Table 1, none are hard-coded.

## 2.1. Planetary Orientation and Orbit

[25] KRC can accept either fixed heliocentric range and subsolar latitude, or Keplerian orbital elements and a fixed pole-orientation (direction of the spin axis); in both cases, “seasons” are at uniform increments of time. An associated Planetary ORBit program set, **PORB**, main program **porbmn**, accesses files containing the elements for all the planets [Seidelmann *et al.*, 1974] and a few comets and asteroids (straightforward to add more); this program set pre-calculates the orbital elements for any epoch, converts them into rotation matrices for the chosen epoch, and creates a plain-text parameter set that is then incorporated into the input file for KRC. This plain-text parameter set is described in Dataset 4 under PORBCM.INC; the PORB system is available at the KRC website. For TES and the THEMIS modeling done at the start of those investigations, the Martian elements (with respect to Earth’s equator and equinox) were evaluated for epoch 1999; Mars’ spin-axis orientation was based on pre-Viking data, and differed from the current best estimates [Seidelmann *et al.*, 2005] by about  $0.3^\circ$ . Within KRC, the orbital position of Mars is computed for each “season”, yielding the heliocentric range, the sub-Solar latitude, and the seasonal indicator  $L_s$ .

[26] Planetary spin-axis orientations have been updated to Seidelmann *et al.* [2005] and mean elements have been updated to Seidelmann [2005]. Short-term perturbations by the planets are ignored, which can yield errors up to  $0.03^\circ$  in  $L_s$  for Mars [Allison and McEwen, 2000, Figure 2].

[27] The length of a season step is input (units of days) and generally will be a submultiple of a planet’s year; it can be as short as one sol (details of how to do this are in Datasets 7 and 8).

## 2.2. Atmosphere

[28] A goal of the KRC model has been to account for the first-order effects of the atmosphere, while preserving the speed and flexibility to deal with surface effects such as layered materials and sloping surfaces. A complicating factor in treating the atmosphere more fully is that the opacity of Mars’ atmosphere can vary considerably in space and time [Smith, 2004, 2009]; although seasonal- and latitude-dependent opacity can be specified for KRC, only GCMs with surface dust interaction can begin to reactively model this.

[29] KRC uses a one-layer atmosphere that is gray in the visible and thermal wavelength ranges. Radiative exchange with the Sun, space, and the surface determines the model atmosphere energy balance and its temperature variation. The columnar mass (and the surface pressure) can vary with season and surface elevation. A uniformly-mixed dust loading is allowed to modify the visual and thermal opacity. Direct and



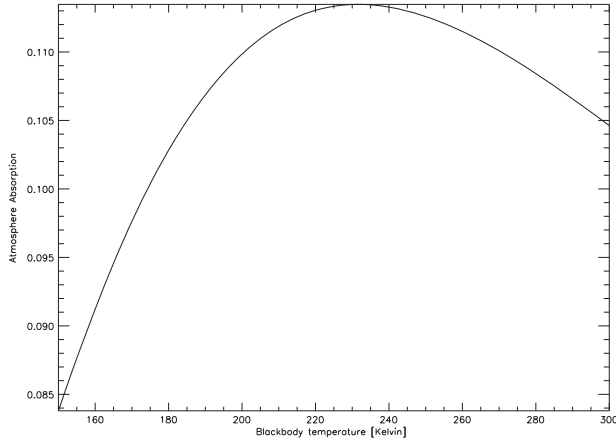


**Figure 1.** Blocking of thermal radiation by a dust-free Mars atmosphere. Shown is the fraction of blackbody radiation absorbed by a nominal atmosphere of 700 Pa CO<sub>2</sub> with a nominal amount of water vapor as a function of surface (blackbody) temperature.

diffuse illumination are computed using a double-precision two-stream Delta-Eddington model, with single scattering albedo  $\varpi$  and Henyey-Greenstein asymmetry parameter  $G_H$ . The thermal opacity due to dust is a constant factor  $C_2$  times the visual dust opacity; this factor is also applied to ice clouds, if considered (a refinement would be to use a separate factor for ice aerosols; the factor is a strong function of particle size for both dust and ice [Clancy *et al.*, 2003]). An option allows an extension of twilight past the geometric terminator.

[30] The current local visible-wavelength (solar) atmospheric opacity of dust can vary with atmospheric pressure; the total (normal) “solar” opacity is  $\tau_v = \tau_0 \cdot P/P_0 + \tau_i/C_2$  where  $\tau_0$  is the unity air-mass visible dust opacity defined for surface pressure  $P_0$ ,  $P$  is the current local surface pressure and  $\tau_i$  is the infrared ice-cloud opacity.  $\tau_0$  and  $\tau_i$  may vary with season and latitude; KRC can ingest a climate model for these two parameters as a function of season and latitude.

### 2.2.1. Delta-Eddington Two-stream

[31] A Delta-Eddington model [Shettle and Weinman, 1970; Joseph *et al.*, 1976] is used for atmosphere scattering and fluxes (**deding2.f**); output parameters are normalized to unit solar irradiance along the incident direction at the top of atmosphere; so they must be multiplied by  $S_M$ , the solar irradiance at the current heliocentric range, to get flux.

[32] Scattering parameters used are the aerosol single scattering albedo  $\varpi$  and the Henyey-Greenstein scattering asymmetry parameter [Joseph *et al.*, 1976]; both are input constants. The computed values include:

Planetary (atmosphere plus surface system) albedo: BOND  
Direct beam at the bottom, includes both collimated and aureole:  $F_{\parallel} = \text{COLL}$   
Diffuse irradiances:  $I_{i,j}$

$i$ : 1 = isotropic, 2 = asymmetric

$j$ : 1 = at top of atmosphere, 2 = at bottom of atmosphere

[33] The net diffuse flux is  $F_{\ominus} = \pi[I_{1j} \pm \frac{2}{3}I_{2j}]$  where + is down,  $F_{\ominus}^{\downarrow}$ ; - is up,  $F_{\ominus}^{\uparrow}$  [Shettle and Weinman, 1970, equation (8)].

[34] The total down-going solar flux at the bottom of the atmosphere is

$$S'_t = S_M (\mu_0 F_{\parallel} + F_{\ominus}^{\downarrow}) \quad (1)$$

where  $\mu_0 \equiv \cos i_0$ ,  $i_0$  is the incidence angle onto a horizontal plane and the diffuse component is  $F_{\ominus}^{\downarrow} = \pi(I_{1,2} + \frac{2}{3}I_{2,2})$ .

[35] Solar heating of the atmosphere, by conservation of energy, is

$$H_V = S_M (\mu_0 - F_{\ominus}^{\uparrow}(0) - (1 - A) [\mu_0 F_{\parallel} + F_{\ominus}^{\downarrow}(\tau_v)]) \quad (2)$$

where  $A$  is the surface albedo.

### 2.2.2. Twilight

[36] Twilight is allowed to account for a turbid atmosphere. It is implemented as having the diffuse downward illumination depend upon an incidence angle scaled to go to 90° when the Sun is  $\text{TWILIGHT} = \eta$  below the geometric horizon. That is, the incidence angle input to the Delta-Eddington routine for diffuse downward illumination is  $\frac{90}{90+\eta} i_0$ .

[37] Because of the twilight extension, a small negative energy balance near twilight can remain. Physically, this is lateral scattering and does not strictly fit a one-layer model. There is no solar heating of the atmosphere during twilight.

### 2.2.3. Atmospheric IR Radiation

[38] The IR opacity is approximated as  $\tau_R = P/P_0 \cdot (C_1 + C_2\tau_0) + \tau_i$  where  $C_1$  represents the opacity of the “clear” (no dust or ice aerosols) atmosphere, primarily due to the 15  $\mu\text{m}$  CO<sub>2</sub> band, and  $C_2$  is the IR/visual opacity ratio for dust [e.g., Martin, 1986].

[39] To estimate the down-going radiation from a clear atmosphere, a synthetic transmission spectrum of the Mars atmosphere with a nominal amount of water vapor (provided by David Crisp, 700 Pa column) was multiplied by blackbody spectra for a range of temperatures to determine the fraction of radiation blocked (see Figure 1). A coefficient of  $C_1 = 0.11 \pm 0.004$  covers the range from 187 K to 293 K; a first-order correction for other surface pressures is to scale this input parameter linearly with the chosen total pressure  $P_0$ .

[40] The fractional thermal transmission of the atmosphere at zenith is roughly  $e^{-\tau_R}$ . The fractional absorption is  $\beta \equiv 1 - e^{-\tau_R}$ .

[41] The fractional transmission of planetary (thermal) radiation in a hemisphere is

$$e^{-\tau_e} \equiv \int_0^{\pi/2} e^{-\tau/\cos \theta} \cos \theta \sin \theta \, d\theta \quad (3)$$

[42] Numerical integration shows that the effective hemispheric opacity is, within about 0.05 in the factor,

$$\tau_e \sim [1.0 < (1.50307 - 0.121687 * \ln \tau_R) < 2.0] \tau_R; \quad (4)$$

this is used in the effective absorption  $\beta_e \equiv 1 - e^{-\tau_e}$ .

[43] The hemispheric downward (and upward) emission from a gray slab atmosphere is:  $R_{\psi} = \sigma T_a^4 \beta_e$ ;  $\sigma$  is the Stephan-Boltzmann constant. The IR heating of the atmosphere is

$$H_R = \epsilon \sigma T_s^4 (1 - e^{-\tau_e}) - 2R_{\psi} = \sigma \beta_e (\epsilon T_s^4 - 2T_a^4) \quad (5)$$

where  $\epsilon$  is the surface emissivity.

## 2.2.4. Atmospheric Temperature

[44] The atmospheric temperature is assumed to follow radiative energy conservation

$$\frac{\partial T_a}{\partial t} = \frac{H_R + H_V}{C_p M_a} \quad (6)$$

where  $M_a = P/g$  is the mass of the atmosphere and  $C_p$  is its specific heat at constant pressure.

[45] Because the atmospheric temperature variation has significant time lag relative to the surface (typically about 1/4 sol, as will be seen in Figures 5 and 6), KRC uses the surface temperature from the prior time step (typically 1/384 of a sol) to evaluate  $H_R$  with little error (effect on  $T_a$ : average:  $<0.2K$ , amplitude:  $<0.5\%$ , phase:  $<1^\circ$ ).

[46] If the computed atmospheric temperature at midnight drops below the  $\text{CO}_2$  saturation temperature (“frost point”) at one scale height above the local surface, it is bounded at this value and the excess energy loss is converted to snow. If there is frost on the ground, this snow mass is added to the frost; otherwise, it is ignored in the heat budget, which strictly does not conserve energy. (Occurs near the edge of the north cap, typically for one season step. Maximum rate about  $\Delta M$  0.5 kg/m<sup>2</sup> per sol, equivalent to  $\Delta T_a$  2.5 K change in atmosphere temperature.)

$$\Delta M = \Delta T_a c_p M_a / L \quad (7)$$

[47] The nadir planetary brightness temperature is given by

$$\begin{aligned} \sigma T_P^4 &= \epsilon \sigma T_S^4 (e^{-\tau_R}) + \sigma T_a^4 (1 - e^{-\tau_R}) \\ \Rightarrow T_P &= [\epsilon(1 - \beta) T_S^4 + \beta T_a^4]^{1/4}. \end{aligned} \quad (8)$$

## 2.3. Geometry and Starting Conditions

### 2.3.1. Geometry

[48] The diurnal variation of insolation onto the surface at the bottom of the atmosphere is computed for the current season and latitude. The incidence angle from zenith onto the horizontal plane ( $i_0$ ) or sloped surface ( $i_2$ ) [rising above an extended plane] is computed by:

$$\cos i_0 = \mathbf{N} \cdot \mathbf{H} \quad \text{OR} \quad \cos i_2 = \mathbf{N}_2 \cdot \mathbf{H} \quad (9)$$

Where  $\mathbf{N}$  is the ellipsoid normal,  $\mathbf{N}_2$  is the local surface normal and  $\mathbf{H}$  is the vector from Mars to the Sun. For these vector operations, a coordinate system with  $Z$  along the planet’s north spin axis and  $X$  in the meridian of the virtual surface point (the meridian at the appropriate hour from midnight) is used. Slope is specified by dip and down-slope azimuth (going eastward from north) (Prior to June 2012 the relation  $\cos i_2 = \sin \delta \sin(\theta + s_N) - \cos \delta \cos(\theta + s_N) \cos(\phi + s_E)$  was used, where  $\delta$  is the solar declination,  $\theta$  is latitude,  $\phi$  is hour angle from midnight,  $s_N$  is the north component of surface slope, and  $s_E$  is the east component of surface slope.)

[49] Direct (collimated) insolation is computed for the local surface, which may be sloped in any direction and has incidence angle  $i_2$ .

[50] Direct insolation is zero when either  $i_0$  or  $i_2$  is  $>90^\circ$ . Diffuse illumination is based on  $i_0$ , with the optional extension into twilight (see section 2.2.2). For a sloped surface, the solid angle of skylight is reduced and light reflected off the regional surface (presumed Lambert and of the same albedo) is added; the Delta-Eddington downward

diffuse radiance is multiplied by  $\text{DIFAC} = 1 - \alpha + \alpha A$ , where  $\alpha = (1 - \cos i_2)/2$  is the fraction of the upper hemisphere obscured by ground. For the bottom of conical depressions,  $\alpha = \sin^2(\frac{\pi}{2} - s)$  where  $s$  is the slope up to the apparent horizon (see section 2.5.2).

[51] If a sloping surface (or pit) is used, the regional horizontal surface (or pit wall) is assumed to be an IR source of solid angle  $\alpha 2\pi$  at the same temperature,  $T_s$ ; this becomes a poor approximation for steep slopes.

[52] The incident flux at the top of the atmosphere is:  $I = S_M \cos i_0$ , where  $S_M \equiv \frac{S_0}{U^2}$ ,  $S_0$  is the solar constant and  $U$  is heliocentric range of Mars in astronomical units.

### 2.3.2. Starting Conditions: Diurnal-Average Equilibrium

[53] For the first season, the atmosphere temperature is set based on the equilibrium for no net heating of the atmosphere or surface, using the diurnal average of insolation (see equations (2) and (5))

$$\langle H_V \rangle + \langle H_R \rangle = 0 \quad (10)$$

[54] Surface radiation balance, from equation (13) for a flat surface with no net subsurface heat flow:

$$\epsilon \sigma \langle T_s^4 \rangle = (1 - A) \langle S_{(t)} \rangle + \epsilon \sigma \beta_e \langle T_a^4 \rangle \quad (11)$$

[55] Expansion of  $\langle H_R \rangle$  using equation (5) and a combination of equations (10) and (11), yields

$$\langle T_a^4 \rangle = \frac{\langle H_V \rangle / \beta_e + (1 - A) \langle S_{(t)} \rangle}{\sigma(2 - \epsilon \beta_e)} \quad (12)$$

[56] For computational simplicity, the average top-of-atmosphere insolation is used as an approximation for  $\langle S_{(t)} \rangle$ ; this slightly overestimates the temperature of the atmosphere at the start of the first season.  $\langle T_s \rangle$  is then derived using (11) to get all layer starting temperatures for the first season, unless starting temperatures are specified by the input parameters.

[57] For the first season, input value  $T_{\text{ATM}}$  is used to get a scale height for surface pressure calculations; thereafter, the diurnal average of  $T_a$  for the prior season at the current latitude is used. All atmosphere-related approximations are quickly attenuated during spin-up.

## 2.4. $\text{CO}_2$ Frost Condensation and Sublimation

[58] The local frost condensation temperature  $T_{\text{FNOW}}$  may be either fixed at an input value  $T_{\text{FROST}}$ , or derived from the local surface partial pressure at the current season.

[59] The relation between condensation/sublimation temperature and partial pressure is taken to follow an approximation adequate for Martian surface conditions:  $\ln P_c = a - b/T$ , in **CO2PT** with  $a = 27.9546$ ,  $b = 3182.48 \text{ K}^{-1}$  and  $P_c$  in Pascal, as given in *James et al.* [1992].

[60] If frost is present,  $E = W \cdot \Delta t$  energy is used to modify the amount of frost  $M$  (kg/m<sup>2</sup>),  $W$  is the net heating at the surface defined in equation (13) and  $\Delta t$  the duration of an single time step;  $\Delta M = -E/L$ , where  $L$  is the latent heat of sublimation. The frost albedo may depend upon insolation, and there may be an exponential attenuation of the underlying

ground albedo (see section 2.4.1). Both frost albedo and  $\Delta M$  are computed at each time step. The amount of frost at each latitude is carried (asymptotic prediction, see section 3.2.7) to the next season.

#### 2.4.1. Effective Albedo

[61] A thick frost deposit can have a constant albedo, or be linearly dependent upon the insolation as described by *Paige* [1985] and *Kieffer et al.* [2000]. It should be noted that it is now known that regions of the seasonal caps can have virtually constant low albedo [*Kieffer et al.*, 2000; *Titus et al.*, 2001].

[62] As the seasonal frost thins (or thickens), the effective albedo of the surface can continuously approach that of underlying soil.  $A = A_f + (A_s - A_f)e^{-M/M_e}$  where  $A_f$  is the albedo of a thick frost,  $A_s$  is the albedo of the underlying surface, and  $M_e$  is the frost required,  $\text{kg m}^{-2}$ , for unity scattering attenuation. This avoids an unrealistic discontinuity in surface energy balance for a tiny amount of frost.

#### 2.4.2. Global and Local Pressure

[63] The total amount of atmosphere is set by the annual mean surface pressure at the reference elevation,  $P_0$ , input as PTOTAL.

[64] The current global pressure  $P_g = \text{PZREF}$ , can be any of the following, based on the setting of KPREF:

(0) constant at  $P_0$

(1)  $P_0$  times the normalized Viking Lander pressure curve computed in **VLPRES** and based on the average of the three seasonal curves in *Tillman et al.* [1993].

(2) Based on depletion of atmospheric  $\text{CO}_2$  by growth of frost caps;  $P_0$  minus the total frost mass at the end of the prior season. In this case, the input value PTOTAL is not the annual-average pressure at zero elevation but the global average of the atmosphere plus cap system. This option requires that a reasonable number of polar latitudes be included; KRC allows this option only if the number of latitudes NLAT > 8.

[65] The initial partial pressure of  $\text{CO}_2$  at zero elevation is  $P_{c0} = P_0 \cdot (1 - \text{noncondensing fraction}) = \text{PCO2M}$ . The current  $\text{CO}_2$  partial pressure at zero elevation is  $P_{cg} = P_{c0} + (P_g - P_0) = \text{PCO2G}$ .

[66] Both the current local total pressure and  $\text{CO}_2$  partial pressure scale with surface elevation and scale height:  $P \propto e^{-z/\mathcal{H}}$ . The scale height is:  $\mathcal{H} = T_a \mathcal{R} / \mathcal{M}g$ ; where  $T_a$  is the mean atmospheric temperature over the prior day (or season),  $\mathcal{R}$  is the universal gas constant,  $\mathcal{M}$  is the mean molecular weight of the atmosphere (43.46), and  $g$  is the Martian gravity.

[67] Local current dust opacity scales with local total pressure:  $\tau = \tau_0 \cdot P/P_0$  under the assumption that dust is well-mixed in the atmosphere. The atmospheric saturation temperature is evaluated at one scale height above the local surface; if  $T_a$  would fall below this value, condensation is assumed to take place to provide the energy required to prevent this, and the snow is added to the surface frost budget.

## 2.5. Boundary Conditions

### 2.5.1. Level Surface

[68] The surface condition for a frost-free level surface is

$$W = (1 - A)S'_{(t)} + \Omega \epsilon R_{\downarrow} + k \frac{\partial T}{\partial z}(z=0) - \Omega \epsilon \sigma T^4 \quad (13)$$

where  $W$  is the heat flow into the surface,  $A$  is the current surface albedo,  $S'_{(t)}$  is the total solar radiation onto the surface as in equation (1),  $R_{\downarrow}$  is the down-welling thermal radiation (assumed isotropic),  $T$  is the kinetic temperature of the surface,  $k$  is the thermal conductivity of the top layer.  $\Omega$  is the visible fraction of the sky,  $\epsilon$  is the surface emissivity and  $\sigma$  the Stefan-Boltzmann constant. In the absence of frost, the boundary condition is satisfied when  $W=0$ . Most constant terms are precomputed, see Table 1.

[69] When frost is present, the values in equation (13) are replaced with  $\epsilon_F$ ,  $A_F$ , and  $T_F$ , where subscript “F” indicates the frost values, and no iteration is done; leaving  $W$  as a non-zero quantity to change the mass of frost on the ground as discussed in section 2.4.

### 2.5.2. Slopes and Conical Depressions

[70] A single one-dimensional thermal model has a modest ability to account for nonflat geometry. The solar and thermal radiation fields are modified for a planar sloped surface or for the bottom of a circular depression (here termed a “pit”, although the geometry applies to any scale). The collimated incident beam is treated rigorously, intensities of the diffuse solar and thermal fields are modified by the fraction of sky visible, and the average reflectance and emittance of the surrounding surface (absent in the level case) are approximated as: the brightness of level terrain with the same albedo, and material having the same temperature as the target surface, respectively; this last approximation accentuates the diurnal surface temperature variation with increasing slope. Then

$$S'_t = S_M \left[ F_{\parallel} \cos i_2 + \Omega F_{\odot}^{\downarrow} + \alpha A \left( G_1 F_{\parallel} + \Omega F_{\odot}^{\downarrow} \right) \right] \quad (14)$$

$F_{\parallel}$  is the collimated beam in the Delta-Eddington model and  $F_{\odot}^{\downarrow}$  is the down-going diffuse beam.  $\Omega \equiv 1 - \alpha$  here and in equation (13).  $G_1$  is the fraction of the visible surrounding surface which is illuminated. Within the brackets in equation (14),

The first term is the direct collimated beam, **DIRECT**

The second is the diffuse skylight directly onto the target surface, **DIFFUSE**

The third term is light that has scattered once off the surrounding surface, **BOUNCE**

[71] For a sloped surface,  $G_1$  is taken as unity. As a first approximation, for depressions  $G_1 = (90 - i)/s < 1$  where  $s$  is the slope to the lip of the depression (the apparent horizon). For the flat-bottom of a depression,  $i_2 = i_0$  when the Sun is above this slope, and  $\cos i_2 = 0$  when below.

### 2.5.3. Physical Properties, Layering of Materials, and Subsurface Scaling

[72] For a homogeneous, semi-infinite material with temperature-independent properties under a periodic insolation of angular frequency  $\omega$ , the amplitude of the surface temperature variation is proportional to  $1/\sqrt{\omega} \cdot 1/\sqrt{k\rho C}$  (section 2.6) [*Carslaw and Jaeger*, 1959];  $k$  is the thermal conductivity [W/(K m)],  $\rho$  is the density [ $\text{kg/m}^3$ ], and  $C$

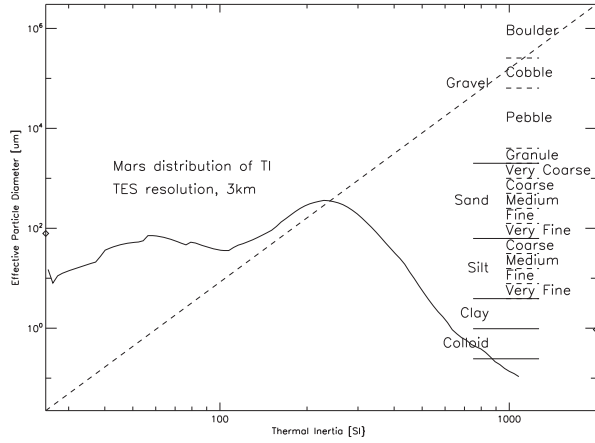


**Figure 2.** Nominal relation between thermal inertia and effective particle size [Presley and Christensen, 1997], shown as the nearly straight dashed line; specific conditions are  $P = 600$  Pascal, density  $\rho = 1600 \text{ kg/m}^3$  and specific heat  $c = 625 \text{ J/(kg K)}$ . The size designations are standard Wentworth scale. The areal distribution of thermal inertia on Mars between latitudes  $65^\circ\text{S}$  and  $70^\circ\text{N}$  is shown as the jagged line, derived from mapping using TES nighttime data of Putzig et al. [2005]; note the log scale, vertical position arbitrary. The bimodal distribution peaks at 60 and 200 (dominant) SI units, corresponding to the low limit for clay (particle diameter  $1 \mu\text{m}$ ) and to medium sand (particle diameter  $0.5$  to  $1 \text{ mm}$ ). Remote-sensing values above about 200 are increasingly affected by rock population or real bedrock [Nowicki and Christensen, 2007].

the volume specific heat  $[\text{J/(kg K)}]$ .  $\sqrt{k\rho C}$  is called the thermal inertia  $I$  of a material and has units  $[\text{J m}^{-2} \text{s}^{-1/2} \text{K}^{-1}]$ . The variation is attenuated into the material as  $e^{-z/D}$  where  $D = \sqrt{\frac{P}{\pi} \cdot \frac{\rho C}{k}}$  is the skin depth and  $P = 2\pi/\omega$  is the diurnal period in seconds. The thermal diffusivity is  $\kappa = \frac{k}{\rho C}$ .

[73] All physical properties are specified by parameters in the input file. Nominal planetary parameters for Mars are the mean solar day, 1.0275 days, and the surface gravity,  $3.727 \text{ m s}^{-2}$ . Properties of the upper-layer material are specified by the thermal inertia, density and specific heat; these in turn set the conductivity (unless temperature-dependent properties are used). Beginning with layer IC, all lower layers can have their conductivity, density, and specific heat reset to COND2, DENS2, and SPHT2, respectively. If LOCAL is set true, then the physical thickness of these layers scales with the local thermal diffusivity; otherwise, the geometric increase of physical layer thickness continues downward unaltered.

#### 2.5.4. Base of Model

[74] Normally, the base of the model is treated as insulating. However, there are also options for it to be held at a fixed temperature, which is useful to model subsurface  $\text{H}_2\text{O}$  ice.

#### 2.6. Relation of Thermal Inertia to Particle Size

[75] The relation of  $I$  to particle diameter is based on laboratory measurements of thermal conductivity:  $k = (c_1 P^{0.6}) d^{-0.11 \ln(P/c_2)}$  [Presley and Christensen, 1997]; where

$c_1 \sim 0.0015$  and  $c_2 \sim 8.1 \times 10^4 \text{ Torr}$  [ $1.08 \text{E}7 \text{ Pa}$ ] are constants. The relation for typical Martian conditions is shown in Figure 2. Also shown in Figure 2 is a histogram of the thermal inertia determined from TES global map data [Putzig and Mellon, 2007], although that map used a different thermal model. The  $I$  source data are available at <http://lasp.colorado.edu/inertia/2007/>; these data were weighted by area. Most areas are in  $I$  range of  $100:500 \text{ J m}^{-2} \text{s}^{-1/2} \text{K}^{-1}$ ; values above about 200 are increasingly affected by a rock population or real bedrock, which has  $I \sim 2000 \text{ J m}^{-2} \text{s}^{-1/2} \text{K}^{-1}$ .

### 3. Numerical Methods

#### 3.1. Basic Method

[76] KRC uses layers that increase geometrically in thickness  $B_i$  by a factor RLAY (this parameter can be set to 1.0 to obtain uniform layer thickness). To simplify the innermost code loops, KRC places the physical radiating surface between the first and second model layers. The layer index  $i$ , increases downward. Below, subscript  $+$  ( $-$ ) is shorthand for  $i+1$  ( $i-1$ );  $i+.5$  is the lower boundary of the layer.

[77] The basic differential equation of heat diffusion is:

$$\frac{\partial T}{\partial t} = \frac{-1}{\rho c} \frac{\partial}{\partial z} \left( -k \frac{\partial T}{\partial z} \right) = \frac{k}{\rho c} \frac{\partial^2 T}{\partial z^2} + \left[ \frac{1}{\rho c} \frac{\partial k}{\partial z} \frac{\partial T}{\partial z} \right] \quad (15)$$

where  $t$  = time,  $T$  = temperature, and  $z$  is the vertical coordinate.

[78] The term in brackets is assumed to be zero within each layer, as is strictly the case for temperature-independent conductivity; the approximation for temperature-dependent  $k$  is discussed in section 3.2.1.

[79] Expressed for numerical calculations

$$\frac{\Delta T_i}{\Delta t} = - \frac{H_{i+.5} - H_{i-.5}}{B_i \rho_i C_i} \quad (16)$$

where  $B_i$  = is the layer thickness and  $H$  = heat flow at the boundary.

[80] The heat flow at interface between two layers is:  $H = -k \frac{\Delta T}{\Delta x}$

$$H_{i+.5} = - \frac{T' - T_i}{B_i/2} k_i \quad \text{or} \quad T' - T_i = - \frac{H_{i+.5} B_i}{2 k_i} \quad (17)$$

where  $T'$  is the temperature at the interface.

$$\text{Similarly} \quad T_{i+1} - T' = - \frac{H_{i+.5} B_{i+1}}{2 k_{i+1}}$$

$$\text{Thus} \quad T_{i+1} - T_i = - \frac{H_{i+.5}}{2} \left( \frac{B_i}{k_i} + \frac{B_{i+1}}{k_{i+1}} \right)$$

$$\text{or} \quad H_{i+.5} = - \frac{2(T_{i+1} - T_i)}{\frac{B_i}{k_i} + \frac{B_{i+1}}{k_{i+1}}}$$

$$\text{Similarly} \quad H_{i-.5} = -2 \frac{T - T_-}{\frac{B}{k} + \frac{B_-}{k_-}}$$

[81] For uniform layer thickness in uniform material, the standard form of explicit forward difference is

$$\frac{\Delta T_i}{\Delta t} = \frac{\kappa}{B^2} [T_+ - 2T_i + T_-]. \quad (18)$$

#### 3.2. Finite Difference Scheme for Exponential Layer Thickness

[82] For variable layer thickness: equation (18) becomes



$$\frac{\Delta T_i}{\Delta t_i} = \frac{2}{B_i \rho_i C_i} \left[ \frac{T_+ - T_i}{\frac{B_i}{k_i} + \frac{B_+}{k_+}} - \frac{T_i - T_-}{\frac{B_i}{k_i} + \frac{B_-}{k_-}} \right] \quad (19)$$

[83] For KRC, formulate this as

$$\Delta T_i = F_{1_i} [T_+ + F_{2_i} T_i + F_{3_i} T_-] \quad (20)$$

[84] KRC defines intermediate constants for each layer:

$$F_{1_i} = \frac{2\Delta t_i}{B_i \rho_i C_i} \cdot \frac{1}{\frac{B_i}{k_i} + \frac{B_+}{k_+}} \equiv \frac{2\Delta t_i}{\rho_i C_i B_i^2} \cdot \frac{k_i}{1 + \frac{B_+}{B_i} \frac{k_i}{k_+}} \quad (21)$$

and

$$F_{3_i} = \left( \frac{B_i}{k_i} + \frac{B_+}{k_+} \right) \cdot \frac{1}{\frac{B_i}{k_i} + \frac{B_-}{k_-}} \equiv \frac{1 + \frac{B_+}{B_i} \frac{k_i}{k_+}}{1 + \frac{B_-}{B_i} \frac{k_i}{k_-}} \quad (22)$$

and

$$F_{2_i} = -(1 + F_{3_i}) \quad (23)$$

[85] Then the innermost loop, one time step for one layer, is equation (20) followed by

$$T_i = T_i + \Delta T_i \quad (24)$$

[86] The input parameter FLAY specifies the thickness of the top “virtual” layer in units of the diurnal skin-depth SCALE, so that the scaled thickness of the uppermost layer in the soil is FLAY\*RLAY, and the physical depth of its center in meters is 0.5\*FLAY\*RLAY\*SCALE. Normally, (LP2 set true) a table of layer thickness, depth, (both scaled and in meters), overlying mass, and numerical convergence factor is printed at the start of a run.

### 3.2.1. Extension to Temperature-dependent Properties

[87] The thermal conductivity of many geologic materials decreases with temperature over all Martian surface temperatures; exceptions are very basic materials (Anorthosite, Obsidian, gabbro) and glasses and fused silica, all of which have  $k$  that is relatively low and can increase with temperature [survey of Birch and Clark, 1940; Horai and Simmons, 1970; Zoth and Haenel, 1988; Cahill et al., 1992; Sass et al., 1992; Clauser and Huenges, 1995; Petrunin and Popov, 1995; Seipold and Huenges, 1998; Vosteen and Schellschmidt, 2003]. Published analytic fits to measurements of bulk materials commonly are in the form  $k = 1/(a + bT)$  or some algebraic equivalent [Horai and Simmons, 1969; Sass et al., 1984; Zoth and Haenel, 1988; Clauser and Huenges, 1995; Vosteen and Schellschmidt, 2003].

[88] The surface of much of Mars and many bodies without an atmosphere is a particulate material whose grains are composed of minerals and glasses. The effective conductivity of these particulates is strongly dependent upon the particle size and increases strongly with gas pressure over a range where the mean-free-path transitions from larger to smaller than the particle (or void) size [Wechsler and Glaser, 1965; Presley and Christensen, 1997; Piqueux and Christensen, 2009a].

[89] Because some Martian surface conditions have such low pressure that the gas mean free path can exceed the particle size (e.g., m.f.p. > 50  $\mu\text{m}$  in soil midday at the top of Olympus Mons), and because it is desirable for KRC to be

able to address vacuum conditions, a form including  $T^3$  is advantageous to treat radiative transfer.

[90] Specific heat increases with temperature for geologic materials and Martian conditions. Theoretical models range from the classic model of Debye [1912] or Kittel [1976, p. 136] to the comprehensive formulation of S.W. Kieffer [Kieffer, 1979]. There are several few-term empirical relations, e.g.,  $\frac{A}{B+T}$ ,  $(T/T_c)^\beta$ , polynomial in  $T - T_c/T_c$  [Ledlow et al., 1992],  $c_1 - c_2/\sqrt{T} - c_3 T^{-2} + c_4 T^{-3}$  where all coefficients are positive [Berman and Brown, 1985], and others in Waples and Waples [2004]. However, it was found that over the full range of Martian temperatures a cubic polynomial would fit geologic materials with error < 1 %.

[91] An informal description of a literature search on thermal properties and the development of code to generate the cubic-polynomial coefficients is contained in Kieffer [2010]. A separate study of the theoretical variation of the effective thermal conductivity of particulate materials as a function of grain-size, cementing and temperature, inspired by the early versions of the numerical modeling of Piqueux and Christensen [2009a, 2009b] was done [Kieffer, 2009]. Both of these are available at the KRC website.

[92] The addition of temperature-dependent properties is a significant variation to the constant-conductivity version because these properties must be evaluated at each layer and time step. The layer setup described in the prior section remains based on the values of the physical properties at a reference temperature, chosen to be 220 K, which is the approximate midpoint of the full range of surface temperatures on Mars.

[93] KRC use the logical flag KOFT to enable temperature-dependence of both conductivity and specific heat, and both are implemented as third-degree polynomials, which minimizes the complexity of the code; any of the first, second, or third degree terms can be left as zero. To minimize round-off problems, the polynomials use a scaled independent variable  $T' = (T - T_{\text{off}}) T_{\text{mul}} = (T - 220.) * 0.01$ . Because KRC allows two materials, the combination of  $k_{(T)}$  and  $C_{(T)}$  requires a total of 16 coefficients (Implemented 2010 Feb). If KOFT is set false, these coefficients are ignored, the equations of section 3.2 are implemented and KRC executes about twice as fast.

[94] Because conductivities and layer thicknesses appear largely as ratios, KRC calculates these as infrequently as possible. With temperature-dependence enabled, KRC computes once per model:

$$F_{C_i} = 2\Delta t_i / (\rho_i B_i^2) \quad \text{and} \quad F_{B_i} = B_+ / B_i \quad (25)$$

[95] Then, for each time step and for each layer compute  $T'_i = (T_i - \text{XOFF}) * \text{XMUL}$ , then

$$k_i = ((c_3 T' + c_2) T' + c_1) T' + c_0 \quad (26)$$

and similarly  $C_i$  with its coefficients. If two materials are involved, the coefficients for the second material are used for the layers below the material contact.

[96] KRC computes once per time step:  $F_{k_i} = k_{i(T)} / k_{+(T)}$ . Then equations (21) and (22) become

$$F_{1i} = F_{Ci} \cdot \frac{k_{i(T)}/C_{(T)}}{1 + F_{Bi}F_{ki}} \quad (27)$$

and

$$F_{3i} = \frac{1 + F_{Bi}F_{ki}}{1 + 1/(F_{ki}F_{B-})}. \quad (28)$$

[97] Equation (23) remains the same, but must be evaluated for every layer and time step.

[98] The approximation associated with ignoring the term in brackets in equation (15) was estimated by running comparative models in which only the layer thickness and number of layer was changed, keeping the depth to the center of the bottom layer identical; these runs indicate that the difference in  $T_s$  between  $T$ -independent and  $T$ -dependent conductivity cases appears to have error  $< 5\%$  for realistic materials and conditions.

### 3.2.2. Solving the Upper Boundary Condition

[99] When there is no surface frost, the net energy into the upper boundary must be zero. From equation (13), find

$$\frac{\partial W}{\partial T} = -k/X_2 - 4\Omega\epsilon\sigma T^3 \quad (29)$$

where  $X_2$  is the depth to the center of the first soil layer. Note that this includes the normal finite-difference assumption that the temperature gradient in the top half of layer 2 is linear. If considering temperature-dependent thermal conductivity, then  $k$  is approximated as that of the top material layer at the end of the prior time step.

[100] The surface kinetic temperature for a balanced boundary condition, equation (13), is iterated with Newton convergence until the change in  $T$ ,  $\delta \equiv \frac{W}{\partial W/\partial T}$ , is  $< \text{GGT}$

If  $|\delta|/T > 0.8$ , it is assumed that the model has gone unstable and it is terminated.

if  $|\delta|/T > 0.1$ , then  $\delta$  is reduced by 70% before the next iteration to improve stability

[101] If frost is present, the unbalanced energy  $W$  is applied to condensation or sublimation.

[102] After determining the surface temperature, the virtual layer ( $i=1$ ) temperature is set to yield the proper heat flow between the surface and the top physical layer ( $i=2$ );

$$\begin{aligned} (T_s - T_1) \frac{\kappa_1}{B_1/2} &= (T_2 - T_s) \frac{\kappa_2}{B_2/2} \\ \Rightarrow T_1 &= T_2 - (1 + 1/\text{RLAY})(T_2 - T_s) \end{aligned} \quad (30)$$

where the diffusivity of the virtual layer is treated as identical to that of the top physical layer.

### 3.2.3. Stability and Time Doubling

[103] The convergence stability criterion is  $\frac{\Delta t}{(\Delta Z)^2} \kappa < \frac{1}{2}$ , equivalent to  $B^2 > 2\Delta t \kappa$ . A convergence safety factor is defined as  $B_i/\sqrt{2\Delta t_i \kappa_i}$ . The code was found to be numerically unstable if this factor is less than about 0.8. The routine will stop with an error message if the safety factor is anywhere less than one. As the layer thickness increases with depth, the routine will repeatedly double the time interval for deeper layers if all the following conditions are met:

The safety factor is larger than 2

The layer is at least the third down

The remaining time intervals are divisible by 2

No more than MAXBOT time doublings will be done

[104] To handle potential large jumps in diffusivity that are allowed between two materials, an initial calculation of the safety factor for the upper layer of the lower material is made without time-doubling. If this does not meet the input convergence factor CONVF, then the thickness of this and all lower layers is increased to be stable with this safety factor. If the thickness of this key layer is overly conservative, then the number of allowed time-doubling in the upper materials is set accordingly.

[105] The numerous input parameters that control the time-depth grid and convergence are based upon extensive testing done during the code development.

### 3.2.4. Starting Conditions

[106] For the first season, the model starts at 18 h with the surface temperature normally set to the equilibrium surface temperature of a perfect conductor as calculated in equation (11). The bottom temperature is also normally set to this value. The input parameter IB allows the option of setting the initial bottom temperature to TDEEP or also the surface temperature to this value; the latter case is useful for studying details of the disappearance of seasonal frost.

[107] Once the top and bottom temperatures are set, all intermediate layer temperatures are set by linear interpolation with depth. The initial atmosphere temperature is always set to the equilibrium values using equation (12).

### 3.2.5. Jump Perturbations

[108] To make model “spin-up” more efficient, the bottom layers can be “jumped” so that their average temperature is the same as the surface average, the condition for no net heat flow with temperature-independent thermal conductivity. A logical flag LRESET is normally false. It is set True on day NRSET or later of the first season if the lower boundary is adiabatic, but never on the last day of calculation in a season or if the lower boundary temperature is fixed.

[109] On a day when LRESET is true, the summation for average layer temperatures,  $\langle T_i \rangle$ , is restarted. At the end of that day, all layer temperatures are offset by  $\langle T_s \rangle - \langle T_i \rangle$  so as to yield no net heat flow.

[110] To help in situations where both diurnal and seasonal temperatures are being addressed, there is an option to instead perturb temperatures based on a linear plus fractional quadratic function of depth between the diurnal average surface and diurnal average bottom temperatures: if DRSET is not zero, then the layer temperature offsets are

$$\Delta T_i = (\langle T_s \rangle - \langle T_n \rangle)(x + \text{DRSET} \cdot x(1 - x)) \quad (31)$$

where  $x = z_i/z_n$  and  $n$  is the bottom layer: some experimentation can help in selecting an effective value of DRSET.

### 3.2.6. Convergence Criteria and Parameters

[111] At each time step, if there is no frost, the surface boundary equation is iterated until the change in surface temperature is less than GGT.

[112] The test for continuing full computations each day into a season is based upon  $\Delta T$ , defined as the RMS change of layer temperatures at midnight, including the virtual layer,

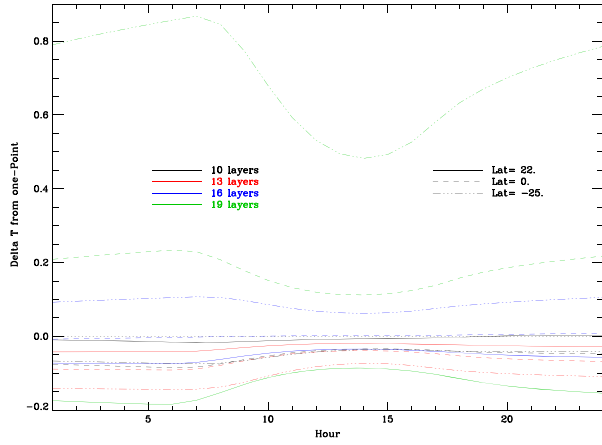


**Figure 3.** Performance of the OnePoint mode with default parameters. Difference in surface temperature of a model with 3 year spin-up with date-steps of  $1/40^{\text{th}}$  Mars year before the final year ending at the  $L_s = 100^\circ$  (northern midsummer), relative to a OnePoint run for  $L_s = 100^\circ$ , for three latitudes (indicated by line type). The 4 year runs had 10, 13, 16, and 19 layers (indicated by color), corresponding to bottom depths of 4.5, 8.5, 15.6, and 27.7 diurnal skin depths. Differences are less than 0.2 K except for the deepest model (with a total thickness greater than an annual skin depth) at a winter latitude when memory of the annual average temperature warms the surface, especially at night.

from midnight the prior day; this is stored at the end of each day in DTMJ.

[113] The test for making the next day the last is: either the temperature change over the last two days is nearly constant, or the temperature change is small; i.e.,

$$\left| 1 - \frac{\Delta_{T,j}}{\Delta_{T,j-1}} \right| \leq \text{DDT} \quad \text{or} \quad \Delta_T \leq \text{DTMAX} \quad (32)$$

where  $\Delta_{T,j-1}$  is forced to be at least  $10^{-6}$ . Normally,  $\text{DDT} = 0.002$ ,  $\text{GGT} = 0.1$  K and  $\text{DTMAX} = 0.1$  K.

[114] After computation of the last day, there is a final check to confirm that convergence has continued: the temperature change has decreased or it is still small; i.e.,

$$\Delta_T \leq \Delta_{T,j-1} \quad \text{or} \quad \Delta_T \leq \text{DTMAX} \quad (33)$$

[115] If these tests fail, and there are days left in the season, then daily calculations are resumed.

### 3.2.7. Prediction to Next Season

[116] Calculations run from midnight to midnight. When convergence has been reached, commonly in fewer days than separate seasons, the results at the last three midnights,  $y_1, y_2, y_3$ , are used to forecast asymptotically the model result at the end of the season,  $y = b_0 + b_1 r^x$  where  $x$  is the number of sols remaining in the season. Normally, this will use a fit over the last three midnights; for convenience reformulated as

$$y = y_3 + c_1(1 - r^x) \quad (34)$$

where  $r = \frac{y_3 - y_2}{y_2 - y_1}$  is the ratio of the last two changes, and  $c_1 = \frac{y_3 - y_2}{(1/r) - 1}$ . If the fit is not asymptotic (e.g., if  $r \geq 1$ ), or if the forecast distance (from the last computed

midnight) is less than 0.9 sols, the routine will do a linear prediction using the most recent two points. In addition, lower and upper limits can be specified, e.g., to keep the temperature from falling below a frost point.

### 3.3. Effect of Spin-up Time, Depth, and Bottom Conditions

[117] Common challenges for large numerical models are initialization and specification of boundary conditions. This section is meant to provide an introduction to this issue, a few specific examples, and to increase awareness of what should be stated in describing a KRC model run.

[118] The default atmosphere has a time constant of a few sols, so that its initial state has little effect on model conditions for runs a modest factor longer than this; e.g., the default OnePoint mode has a 15 sol effective spin-up. Generally, specification of bottom conditions has the largest effect on surface temperature.

[119] KRC has three lower boundary condition options; the first is the default.

- $IB = 0$  All layers start at the equilibrium temperature for the starting season. The boundary is insulating and after a few sols all layers are “jumped” to have the same average as the surface.
- $IB = 1$  The top layer starts at the equilibrium temperature and the bottom at TDEEP, intermediate layer temperatures are linear with depth. The bottom boundary is insulating and no jump is done.
- $IB = 2$  All layers start at TDEEP and the lower boundary is held at this value. This is useful for spring frost recession details. The effect on  $T_s$  compared to setting  $IB = 1$  diminishes with a time-constant of the model total thickness.

[120] Effects on  $T_s$  related to bottom conditions generally are largest predawn, when insolation has the least influence. An example is shown in Figure 3, which illustrates the difference in  $T_s$  of a 3 year spin-up relative to the OnePoint mode; both models run with  $IB = 0$ ; the differences at dawn are about twice the amount at midday.

[121] For three latitudes (VL-1, equator and 25 S) at  $L_s = 100^\circ$ , short and long spin-up time were tried; 20 sols and  $3\frac{1}{4}$  Mars years, with three sets of lower boundary conditions and 10, 13, 16, 19, and 29 layers, corresponding to total model thicknesses of 4.5, 8.5, 15.6, 27.7, and 177 diurnal skin-depths; the last two correspond to 1.1 and 6.8 annual skin-depths. TDEEP was set to 180 K, intentionally about 20 K below the annual average of  $T_s$ ; with this large initial offset there is some residual effect for deep models with  $IB = 2$  even after 4 years. The seasonal excursions of  $T_s$  at 25 S, with a zenith noon Sun near perihelion, are about triple those at VL-1. The diurnal results are shown in Figure 4.

[122] In these examples, the effect of deep-layer memory on  $T_s$  near midday and in the atmosphere at all hours is less than at predawn, both by roughly a factor of 0.6.

[123] If realization of annual effects is desired, a reasonable choice is  $IB = 0$ , with a total thickness of about 25 diurnal skin-depths (1 annual skin-depth), starting near an equinox, and a spin-up of about 2 years.



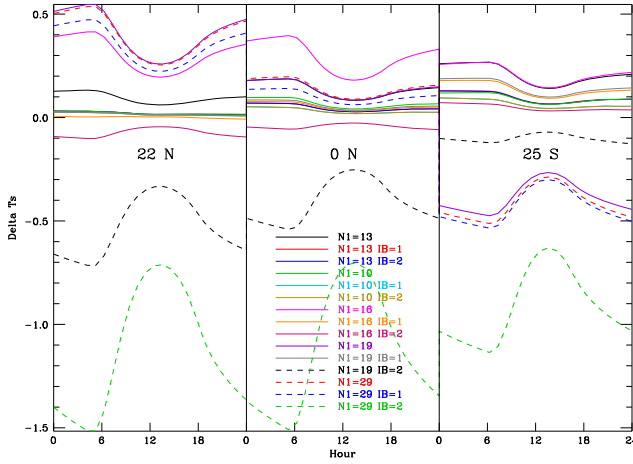


**Figure 4.** Surface temperature  $T_s$  for 20 sol spin-up relative to 3 year spin-up for three latitudes at  $L_s = 100^\circ$ . Cases were run with different total number of layers,  $N1$ , and different lower boundary conditions indicated by the flag  $IB$  as described in section 3.3. The left one-third of the plot shows diurnal results at  $22^\circ\text{N}$ , the middle third at  $0^\circ$ , and the right at  $25^\circ\text{S}$ . Cases that are not apparent are covered by the lines of the next case; e.g.,  $N1 = 10$   $IB = 1$  is obscured by  $N1 = 10$   $IB = 2$ .

### 3.4. Comparison to Other Thermal Models

[124] All planetary thermal models involve some approximations and assumptions. A comparison between their results provides an estimate of these approximations. All models discussed here produce surface kinetic temperature. KRC and the Mellon model [Mellon *et al.*, 2000] are designed for use with remote IR observations and routinely produce net up-going radiation at the top of the atmosphere. The Vasavada model [Vasavada *et al.*, 1999] is designed to define the surface environment and the Ames model [Haberle *et al.*, 1993] is a full GCM. Time shifts of up to 1/2 h may result from precisely how the various models generate the comparison products.

[125] Surface temperatures  $T_s$  of the Vasavada and Mellon models agree closely with KRC; the AMES GCM  $T_s$  is generally cooler due to a deep subsurface starting at below the annual average temperature that would require many model years to reach equilibrium.

[126] Mellon models provide perhaps the best indication of difference in  $T_s$  results between one-layer and multilayer atmosphere; Mellon  $T_s$  is generally a few kelvin cooler than KRC during the day and about 7 K cooler predawn.

[127] The down-going thermal radiation has smaller diurnal variation in KRC than in more detailed atmosphere models; this IR radiation is generally about an order of magnitude smaller than the insolation (note factor of 10 in auxiliary axis scales for Figures 5 and 6).

[128] KRC atmosphere temperatures have similar phase and somewhat larger diurnal amplitude as the mass-weighted product of the Ames GCM. The phase and amplitude of down-going IR flux are also similar, but fluxes are considerably larger in KRC unless a lower infrared/visual opacity ratio is used. More detailed discussion is in the following subsections.

#### 3.4.1. Comparison to Ames GCM

[129] As a check on atmosphere temperatures and down-going radiance, a specific test case was chosen for comparison of the KRC one-layer atmosphere with the multilayer radiative, conductive and convective-coupled atmosphere of a full GCM [Haberle *et al.*, 1993]; the Viking-1 landing site, Latitude  $22^\circ\text{N}$ , elevation  $-3.1$  km,  $L_s = 100^\circ$ ,  $\tau_v = 0.3$ , visible/IR opacity ratio 1.0, surface pressure of 7 mbar, bolometric albedo of 0.25, thermal inertia  $270 \text{ J m}^{-2} \text{ s}^{-1/2} \text{ K}^{-1}$ , soil density  $1600 \text{ kg/m}^3$ , soil specific heat  $630 \text{ J/kg}$ , model depth 40 m. This special GCM run inhibited lateral atmospheric dynamics and output a mass-weighted atmosphere temperature; it started with an isothermal profile at 180 K and was “spun up” for 20 sols before the output date (data kindly provided by Robert Haberle).

[130] The resulting temperatures and fluxes are shown in Figure 5, along with those for three KRC runs. The KRC base model used the parameters shown in Dataset 8, apart from the values listed above, use of 29 layers, and having the bottom at 8 m held at 180 K to approximate the effect of the deeper GCM subsurface; the diurnal skin-depth is 45 mm.

[131] The KRC and GCM atmospheric temperatures have similar mean, variation, and phase, with minima near 8 h and maxima near 17 h; however, the KRC down-going infrared radiance lags the GCM slightly, as expected because the GCM near-surface atmospheric layers dominate the down-going flux and they track the surface temperature more closely than the KRC one-layer atmosphere.

[132] The KRC atmosphere down-going infrared radiances are similar in diurnal behavior but larger than the GCM; use of the KRC default value of 0.5 for IR/visible opacity ratio results in values closer to the GCM, with modest changes

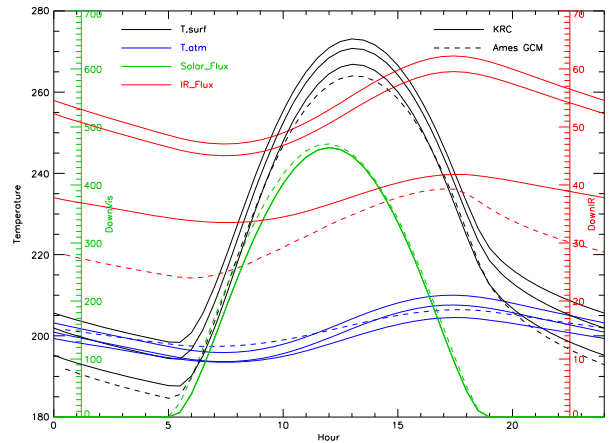


**Figure 5.** Comparison of KRC results (solid lines) to Ames GCM results (dashed lines). Calculations for the Viking Lander 1 site at  $L_s = 100^\circ$  for albedo = 0.25,  $TI = 270$ ,  $\tau = 0.3$  and  $\tau_{\text{IR}}/\tau_{\text{vis}} = 1.0$ . The surface kinetic temperature [black]; mass-weighted temperature of the atmosphere [blue]; down-going infrared radiation at the surface (red, right auxiliary axis), and down-going total insolation at the surface (green, left auxiliary axis). Three KRC runs are shown: the middle for each parameter is with the same input values as the GCM; the lower has  $\tau_{\text{IR}}/\tau_{\text{vis}} = 0.5$ , the KRC default; and the upper starts with equilibrium temperatures and allows the bottom temperature to jump to overcome the unrealistic cold GCM initial conditions.



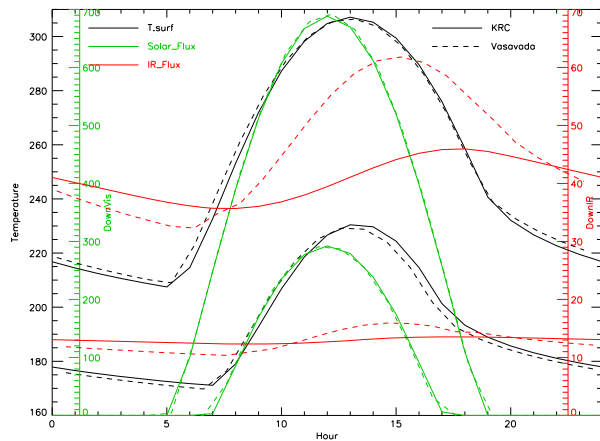


**Figure 6.** Comparison of KRC (solid lines) with thermal model computed by Ashwin Vasavada (dashed lines). Models are for Holden Crater, a location in the final 4 for MSL; latitude 26.37S, elevation  $-94$  km, albedo = 0.13,  $I = 350$ ,  $\tau_0 = 0.1$ . Two seasons are shown:  $L_s = 91^\circ$  and  $270^\circ$ , which correspond to aphelion winter (curves confined to lower half of figure) and perihelion summer (curves rise into upper half of figure). Shown are the surface temperature [black], down-going total insolation at the surface [green, left auxiliary axis], and down-going infrared radiation at the surface [red, right auxiliary axis].

in  $T_s$  and  $T_a$  (lower set of curves in Figure 5).

[133] The GCM surface temperatures are lower than base KRC model by 5–9 K, due in part to initializing all layers at a temperature about 40 K below the surface average. A KRC model with realistic deep temperatures has  $T_s$  and  $T_a$  a few kelvin higher and 5% higher IR flux (upper set of curves in Figure 5).

#### 3.4.2. Comparison to Vasavada Model

[134] Ashwin Vasavada developed a model used at Jet Propulsion Laboratory (JPL) for Martian surface environments. It incorporates temperature-dependent heat capacity and has the ability to model sloped surfaces. The subsurface portion is based on *Vasavada et al.* [1999] and the atmosphere interaction is based on a one-dimensional version of the radiative transfer and boundary layer physics from the Geophysical Fluid Dynamics Laboratory (GFDL) Mars GCM, circa 2004 [Wilson and Hamilton, 1996; Richardson et al., 2002; Basu et al., 2004] and includes basic  $\text{CO}_2$  condensation. There is no geothermal heat flux.

[135] Vasavada provided his results for Holden Crater, a candidate landing site.  $A = 0.13$ ,  $I = 350$  (near 200 K), the thermal emissivity is 0.98. The model assumes a constant 10 m/s wind for the boundary layer. After a few years of spin-up and equilibration, the model output values at 15 min time steps for a Martian year. Surface kinetic temperature, down-going solar and down-going thermal radiation at 1 h intervals were supplied. Comparisons are shown for two seasons in Figure 6;  $T_s$  and solar flux compare closely. The Vasavada down-going thermal radiation is greater and has greater amplitude than KRC, the phase relation to KRC is similar to that for the Ames GCM.

#### 3.4.3. Comparison to Mellon Model

[136] For TES standard processing, Mellon models were generated at 8 sol intervals and  $5^\circ$  latitude spacing for 10

thermal inertia's spaced logarithmically; for three sets of albedo, three sets of dust opacity, and three sets of average surface pressure. Mellon uses a multilayer radiative-convective atmosphere [Mellon et al., 2000] and this model takes about two orders of magnitude longer to run than KRC (M. T. Mellon, personal communication, 2011). KRC models were generated on the same grid; the same values were used for all physical parameters identified in the Mellon model file headers. Mellon models were spun-up for 2 years before the output year [Mellon et al., 2000] and KRC for 3 years before the output year. The diurnal surface temperature curves for three thermal inertias and three latitudes are shown in Figure 7. KRC  $T_s$  is a few degrees warmer, the greatest at night and for low thermal inertia. A seasonal comparison of  $T_b$  is shown in Figure 8; the models track each other closely except for the lowest thermal inertia at  $30^\circ\text{S}$  near  $L_s = 90^\circ$ , when  $\text{CO}_2$  frost forms in only the Mellon model.  $T_b$  for the two models are even closer, and this is the value normally compared to remotely observed temperatures. Mellon  $T_b$  are generally slightly higher than KRC at midday and 0 to 4 K cooler predawn. Differences are largest for the lowest thermal inertia and have smooth variation with season unless  $\text{CO}_2$  frost forms.

## 4. Effect of $T$ -Dependent Properties

[137] Temperature-dependent properties have been considered as contributing to some of the “anomalous” thermal behavior observed on Mars, but not quantified [Ditteon, 1982]. Here, the effect of  $T$ -dependent properties on Mars surface temperature is assessed using realistic properties; the effect was found to be at most a few K. Although it can be assessed in detail with KRC, this complication may rarely be needed.

[138] A test of the temperature-dependent code is to invoke it when the properties have no temperature dependence. The effect on  $T_s$  was measured for latitudes  $0^\circ$  and  $40^\circ\text{S}$  (which

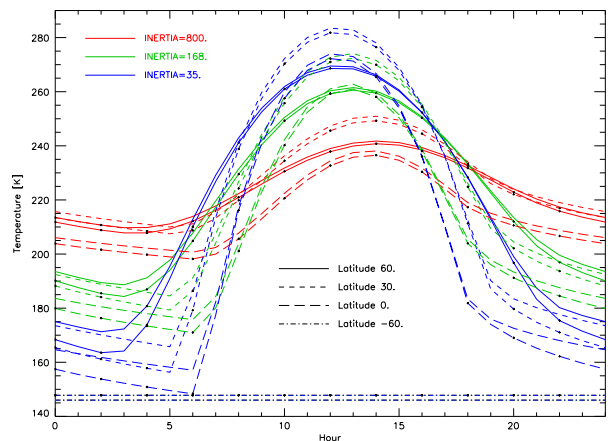


**Figure 7.** Comparison of KRC with the Mellon models (curves with spaced small symbols) used for TES standard production;  $T_s$  surface kinetic temperature. Diurnal curves for TI of 35, 168, and 800 for latitudes  $60^\circ\text{S}$ ,  $0^\circ$ ,  $30^\circ\text{N}$  and  $60^\circ\text{N}$ , all at  $L_s = 100^\circ$ . Both models had seasonal frost all day long at  $60^\circ\text{S}$ . KRC surface temperatures are a few degrees warmer, the greatest at night and for low thermal inertia.

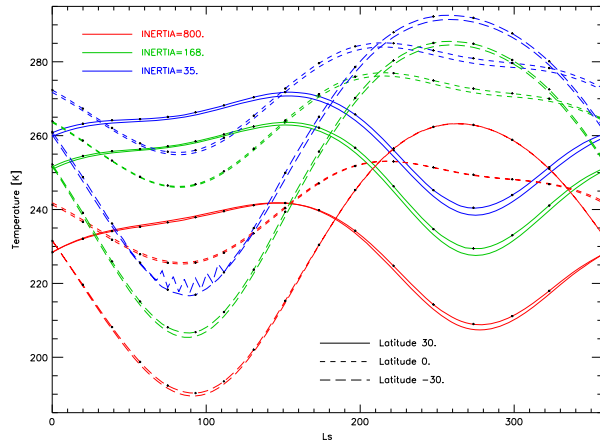


**Figure 8.** Comparison of KRC with the Mellon models used for TES standard production;  $T_b$  planetary bolometric temperature. Seasonal curves for TI of 35, 168, and 800 for latitudes 30°S, 0° and 30°N, all at 13H. The models track each other closely except for the lowest thermal inertia at 30°S near  $L_s=90^\circ$ , when CO<sub>2</sub> frost forms on some nights in the KRC models. Mellon midday  $T_b$  is slightly higher than KRC except for  $I=800$  at Latitudes 0° and 30°N near  $L_s=90^\circ$ .

has large seasonal variation) over 40 seasons after a 3 year spin-up. For a homogeneous model the mean absolute difference was less than 0.3 milli-Kelvin, for two-materials ( $IC=7$ , 1.6 diurnal skin-depths, 3.5 cm), 0.03 milli-Kelvin.

[139] The effect of temperature-dependent materials on surface kinetic temperature was assessed for homogeneous and two-material cases. The base case has  $A=0.25$ ,  $k=0.013 \text{ W m}^{-1} \text{ K}^{-1}$ ,  $\rho=1600 \text{ kg m}^{-3}$ , and  $C=630 \text{ J kg}^{-1} \text{ K}^{-1}$  yielding  $I=114.5 \text{ J m}^{-2} \text{ s}^{-1/2} \text{ K}^{-1}$ , the lower material has  $k=2.7868$ ,  $\rho=928$ , and  $C=1710.65$  yielding  $I=2103.3$ .

[140] For the homogeneous case, and the upper material in the layered case, the conductivity is that of sediments in *Vosteen and Schellschmidt* [2003] and the specific heat the chlorite of *Bertoldi et al.* [2007]; both scaled slightly to exactly match the above values at  $T=220 \text{ K}$ . These materials have relatively large  $T$  dependence. The lower material is pure H<sub>2</sub>O ice Ih with  $T$ -dependent conductivity and specific heat [Hobbs, 1974].

[141] For latitude 0°, the diurnal behavior is similar all year; the season-averaged results are shown in Figure 9 for temperature-dependent  $k$  and  $c$  individually and together. The effects of  $k$ , which generally decreases with temperature, and  $c$ , which increases with temperature, somewhat offset each other. The results with a lower layer of ice starting at 1.6 diurnal skin-depths (closer to the surface than generally expected for Mars) are little different from the homogeneous case.

## 5. KRC Architecture and Use

[142] KRC is structured so that the main program calls routines to handle the input and setup the output style; it calls a hierarchy of routines to do the calculations for each season, each latitude, and each day (until convergence). This architecture is described in Dataset 1. An index of routines is in Dataset 2 and the code is contained in Datasets 3, 4, and 5.

[143] All the KRC runs for this paper were compiled with the GNU compiler 4.1.2 under a Linux operating system (CentOS 5.4) with 64 bit hardware; a makefile for this system is in Dataset 6. A user's guide is available in Dataset 7.

[144] For normal runs, the user will be prompted for the name of the input file and the name of a print file. All actions are controlled by the input file. Users unfamiliar with KRC or similar models are encouraged to run comparative models with different layer and time step sizes, spin-up times and different convergence parameters to obtain an estimate of numerical accuracy.

### 5.1. Setting the Starting Date

[145] To run KRC with unrecorded “spin-up” seasons

Choose the  $L_s$  of the first output season

Convert that to a full Julian date

Subtract the number of spin-up seasons times the delta-days between seasons

i.e.,  $-(\text{JDISK}-1)*\text{DELJUL}$

Subtract 2,440,000; use this as the starting date DJUL

### 5.2. Input Parameters

[146] The normal print files list for each case all the current changes, then the resulting full set of parameters (excepting the orbital matrix) and the set of latitudes and elevations. Its format is similar to the input file, shown in Dataset 8.

### 5.3. Sample Layer Table

[147] Normally (LP2 true) a layer table is printed at the beginning of each case. This lists the layer thickness and center-depth in both meters and diurnal skin-depth. It also includes the column mass above the center of each layer and the safety factor beyond classical numerical stability. If seasonal memory is not required, then a scaled center

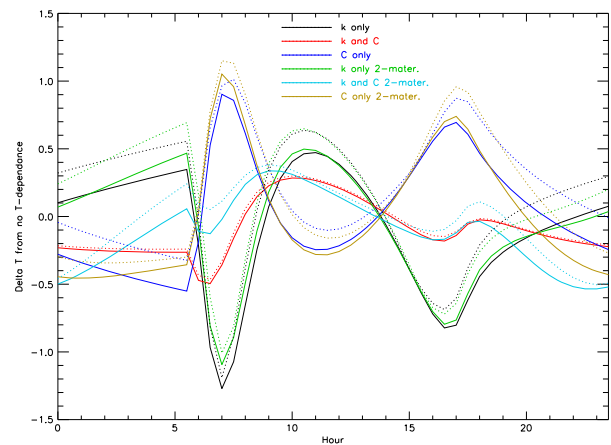


**Figure 9.** Effect of temperature-dependent thermal properties, shown as the diurnal variation of the surface temperature change from a base case with temperature-independent thermal properties; see the text in section 4. Solid lines show the average over 40 uniformly spaced seasons; the dotted lines represent plus one standard deviation. The legend indicates which properties had temperature-dependence for a homogeneous and a two-material case.

depth of order five is adequate. Mars annual skin-depth is 25.85 times the diurnal skin-depth; if the effect of seasonal memory is desired, then the bottom depth should exceed this. An example is shown in Dataset 9.

#### 5.4. Print Output

[148] A record of changes and optional notification of season progress appears on the monitor. A separate print file, default name *krc.prt*, is generated for which there are many options, described in the help-list; Dataset 7. Voluminous output is possible; it is best to start with the defaults in the sample input file, Dataset 8, then experiment with the options for small cases.

#### 5.5. Linked Runs

[149] KRC has the ability to continue from the vertical temperature profile at the end of a prior case, as long as the physical distribution of the layers is not changed. It can also start with the conditions at any season in a prior run stored with *K4OUT* = -1. These can be useful for (at least) two purposes:

[150] 1. By continuing from memory and incrementing the total number of seasons, it is possible to continuously change parameters in addition to the atmospheric opacity and surface albedo (for which seasonal tables may be specified).

[151] 2. Details related to seasonal frost appearance/disappearance. A run-up of a few years with about 40 seasons per year can be used to establish a frost budget and deep temperature profile. Then, the season interval can be set to 1 sol, and events followed in detail.

#### 5.6. One-Point Version: An Alternate Input

[152] To support some detailed THEMIS studies, an interface to the KRC system was built that computes the temperature for a single condition. Two input files are involved:

[153] 1. A “master” file specifying all general parameters for a single case. The last line processed must contain the name of the “point” file.

[154] 2. A “point” file containing formatted lines that each specify the time and conditions at one point; any number of lines are allowed. These values will override those for corresponding items from the master file.

[155] The underlying model is the full version of KRC and each point is run as an independent case, so the order of input points is arbitrary.

[156] The default OnePoint master file, shown in Dataset 10, has parameters similar to the KRC defaults (Dataset 8). It specifies one latitude and a layer extending to about 5 diurnal skin depths, so there is virtually no seasonal memory. Thus, it does not treat the seasonal frost properly, and results near the edge of the polar cap are likely to be unreliable. It sets the KRC system into a reasonable mode for one-point calculations with a spin-up of 15 sols. Many parameters in this file could be safely modified. The values for starting date, latitude, elevation, albedo, thermal inertia, dust opacity, slope, and azimuth are over-ridden by the values in the One-Point file.

[157] The fields in the OnePoint input are:

Ls  $L_S$  season, in degrees

Lat	Aerographic latitude in degrees
Hour	Local time, in 1/24'ths of a Martian Day
Elev	Surface elevation (relative to the aeroid), Km
Alb	Bolometric Albedo, dimensionless
Inerti	Thermal Inertia, in SI units
Opac	Atmospheric dust opacity in the visible
Slop	Regional slope, in degrees from horizontal
Azim	Azimuth of the down-slope direction, Degrees East of North.

[158] The two additional columns in the output file are:

TkSur Surface kinetic temperature  
TbPla Planetary bolometric brightness temperature  
Execution time is about 3.5 ms per point.

## 6. Examples of Use

### 6.1. Annual Average Surface Temperature

[159] A variety of small-scale morphological features on Mars are similar to terrestrial features whose formation involves flow of liquids. These features are geologically young and some are active [Malin and Edgett, 2000; Reiss et al., 2004; Malin et al., 2006; Balme et al., 2006; Mangold et al., 2010]. While some explanations propose dry flow for angle-of-repose slopes, other explanations for both angle of repose and lower slopes invoke obliquity variations, freezing-point suppression for brines, confinement or protection by snow and ice, and local slope orientation and shelter; all these are strongly dependent upon the subsurface temperature.

[160] Average annual surface temperature is a strong constraint on subsurface temperature. Typical Martian dry surface conditions have  $I \sim 200 \text{ J m}^{-2} \text{ s}^{-1/2} \text{ K}^{-1}$ ,  $\rho \sim 1000 \text{ kg m}^{-3}$ ,  $C \sim 603 \text{ J kg}^{-1} \text{ K}^{-1}$ , yielding  $k = 0.063 \text{ W m}^{-1} \text{ K}^{-1}$ ; for regolith  $k \sim 1.5$ ; for  $\text{H}_2\text{O}$  ice near 170 K,  $k = 3.4$ . Estimates of Mars geothermal heat flow range from  $8 \text{ mW/m}^2$  at the north polar cap (NPC) (Phillips et al. [2008], Supporting Information, section 3) through an upper limit of  $19 \text{ mW/m}^2$  under the NPC [Ruiz et al., 2010] to a global value  $\sim 30 \text{ mW/m}^2$  [Zuber et al., 2000]. For the highest of these heat-flow estimates, the geothermal gradients corresponding to the above three materials would be roughly 0.5, 0.02, and 0.01 K/m, respectively. Thus, for a conservative case of 1 m of  $I = 200$  material underlain by regolith, the mean subsurface temperature would be no more than 1 K above the surface annual mean to a depth of at least 26 m.

[161] An example of the use of KRC is to compute the mean annual soil temperature  $\bar{T}_s$  at MGS-TES resolution of about 3 km. Maps of thermal inertia and albedo with  $1/20^\circ$  resolution were derived from maps described in Putzig and Mellon [2007] and available at <http://lasp.colorado.edu/inertia/2007/>. The square-root of the product of day and night thermal inertias was used; day-night differences rise steeply within  $12^\circ$  of the south pole and  $17^\circ$  of the north pole suggesting that they are not quantitatively reliable. For albedo, the average of Mars Year 24, 25, and 26 was used, avoiding the sections of years 24 and 26 that were duplicates of year 25. For both  $I$  and  $A$ , data are null within  $3^\circ$  of the pole, 0.14% of the surface area. Elevation at  $1/20^\circ$  resolution was obtained by rigorous resolution change (every input pixel used exactly once in total) from the



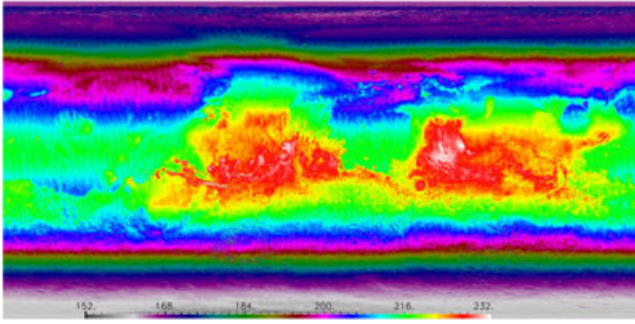


**Figure 10.** Global map of annual-average surface temperature with  $1/20^\circ$  resolution. Based on 711 KRC models run with seasonal dust and ice opacity derived following *Smith* [2009] and interpolated for local bolometric albedo and thermal inertia derived from *Putzig and Mellon* [2007], elevation and surface slope derived from MOLA  $1/32^\circ$  topography. KRC models used 37 latitudes, 8 sol time spacing with a 3 Martian year spin-up. Residual striping is along THEMIS orbital tracks, due to merging data from multiple Mars' years into the albedo and thermal inertia maps. See discussion in section 6.1. Full resolution version in Dataset 12.

MOLA  $1/32^\circ$  resolution data set; file available at <http://pds-geosciences.wustl.edu/missions/mgs/megdr.html>.

[162] Centered slopes in the cardinal directions were obtained by differencing adjacent pixels in the N-S direction and pixels separated proportional to secant of latitude E-W; these slopes have 1.85 km posting. The median slope over 3.7 km is about 0.0057 radians [ $0.326^\circ$ ]; about 0.32% are larger than 0.1 and 0.66% larger than 0.2 radian [5.73 and  $11.46^\circ$ , respectively]. The slope maps were converted to  $1/20^\circ$  resolution ( $\sim 3$  km) by rigorous resolution change.

[163] The seasonal variation of dust and ice-cloud opacity as a function of latitude derived by THEMIS (digital data provided by M. Smith, see *Smith* [2009]) covering 5.3 Mars years was averaged into 1 year, smoothed slightly, and any remaining gaps filled by interpolation; the winter polar regions were filled with  $\tau_0=0.1$  and  $\tau_i=0.001$ . This provided climate maps with  $5^\circ$  resolution in latitude and  $L_s$ , which were then linearly interpolated by KRC. The seasonal pressure variation followed the average of the 3 Viking Lander sites.

[164] KRC was used to generate a model set with level terrain at  $5^\circ$  latitude spacing (except  $\pm 88^\circ$  rather than the true pole) with 8 sol season spacing, output 48 times of day, for all combinations of three albedos ( $A$ ) [0.15, 0.25, 0.35], 15 thermal inertias ( $I$ ) spaced uniformly in logarithm [11, 16, 24, 35, 52, 77, 114, 168, 249, 367, 542, 800, 1181, 1744,  $2575 \text{ J m}^{-2} \text{ s}^{-1/2} \text{ K}^{-1}$ ], and three surface elevations [ $-7.422$ ,  $-1.921$ , and  $5.544$  km] (PTOTAL was 502 Pa and  $T_a=210$ , so that these correspond to surface pressures at  $L_s=0^\circ$  of 1000, 600, and 300 Pa). The KRC system could produce such maps for any slope and azimuth and at current or prior Mars orbital values (obliquity, eccentricity, and longitude of perihelion), although the climate model used here would not be justified.

[165] To accommodate slopes, an additional set of 72 models (omitting every other thermal inertia level) was run with a slopes of 0.1 and 0.2 radians in each of the cardinal directions.

[166] W-E slopes have a small negative effect on  $\bar{T}_s$ , generally less than 0.5 K and roughly quadratic with slope.  $\Delta \bar{T}_s$  has a minimum near  $300 \text{ J m}^{-2} \text{ s}^{-1/2} \text{ K}^{-1}$ . There is little dependence on surface pressure, and an inverse linear relation with  $A$ . S-N slopes have a larger effect, roughly linear with slope magnitude and negative if poleward, changes over  $-70^\circ$  to  $+70^\circ$  latitude are up to 9 K for 0.1 radian slope.

[167] Changes of annual mean temperature from the level model set were used to fit a quadratic form to the E-W and N-S slopes separately. The N-S effect is approximately linear with latitude, being zero near  $+5^\circ$  (due to orbit asymmetry);  $\Delta \bar{T}_s$  is accentuated and erratic over latitudes poleward of  $\sim 45^\circ$  where associated with the seasonal polar cap edge.

[168] For both polar zones, a simple linear interpolation with latitude and with tilt was used for all  $I$ ,  $A$ , and  $P$  combinations. This fit was done to all models after combining all four N:S tilt models normalized by a factor of .5 for the 0.2 tilt runs and by  $-1$  for the south tilt runs. This linear model was applied to one less latitude zone than fit, to provide a reasonably continuous extension.

[169] The resulting global map is shown at reduced resolution in Figure 10. The full binary file is available in Dataset 11. Map values for  $A$  and  $I$  are invalid poleward of  $\pm 87^\circ$ , excluding these regions the area-weighted mean  $\bar{T}_s$  is 206.7 K; omitting regions poleward of  $\pm 70^\circ$ , where results are strongly influenced by the seasonal caps, the mean  $\bar{T}_s$  is 209.2. Northern polar latitudes are largely warmer than southern by several kelvin, as shown in Figure 11.

## 6.2. MSL Landing Site

[170] The MSL landing site is at  $4.5^\circ \text{S}$ ,  $137.4^\circ \text{E}$  on the floor of the crater Gale northwest of the large central mound. The average values for a 15 km square area in this area are  $A=0.215$ ,  $I=313 \text{ J m}^{-2} \text{ s}^{-1/2} \text{ K}^{-1}$ , elev= $-4440$  m (with standard deviations of 0.014, 52, and 60, respectively). The average horizon is elevated at about  $3.5^\circ$ . Using these values, a homogeneous model with emissivity 0.97 was calculated for a Martian year, using a 3 year spin-up; see Figure 12. The elevated horizon increases the average daily surface temperature over somewhat more than half the year, with a maximum of 1.1 K near  $L_s=100^\circ$ ; diurnal average is decreased over  $L_s=190^\circ$  to  $350^\circ$  by up to 0.6 K.

[171] The atmosphere dust and ice opacity in the KRC model followed the THEMIS climate, as described in section 6.1. The effects of opacity variation can be seen as high-frequency perturbations on the smooth seasonal trends; Martian climate is highly variable from year to year so the rapid variations are only indicative of the general nature of dust-storm and ice-cloud effects.

## 6.3. Examples of Polar Frost Budgets

[172] Developing thermal models or GCMs that match the details of seasonal polar caps, let alone the seasonal surface pressure variation, has been challenging. *Wood and Paige* [1992] used a model based on an early version of KRC, but with no topography or aerosol opacity, to match the Viking pressure variation. However, the derived thermal inertia of the surface under the seasonal cap and the derived albedo and emissivity of seasonal frost for various best fits are substantially different from observed values. In a companion



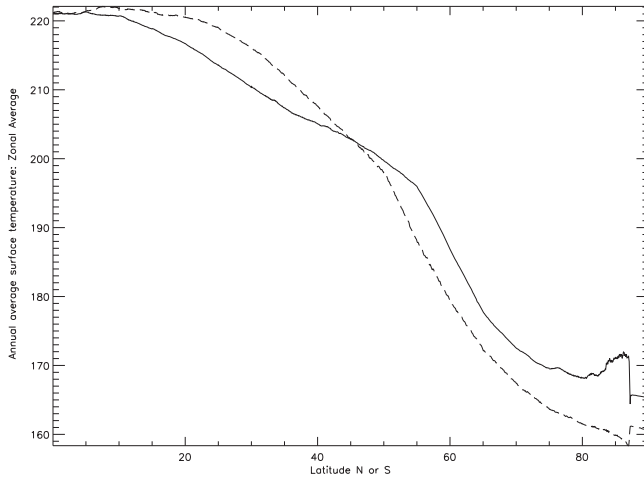


**Figure 11.** Zonal average of annual-average surface temperature. North: solid line; south: dashed line.

paper [Paige, 1992] they included variation of dust opacity and effective frost emissivity to address interannual differences in the seasonal surface pressure.

[173] Recent GCMs include spatial variation of polar surface and frost properties and closely reproduce the Viking pressure measurements [Hourdin *et al.*, 1995; Forget *et al.*, 1998; Haberle *et al.*, 2008; S.L. Lewis, personal communication, 2012]. These models are far more detailed than KRC, but each run of them is a substantial commitment. KRC, with its seasonal cap modeling ability, could be used to easily study the effect of small changes in seasonal-cap parameters.

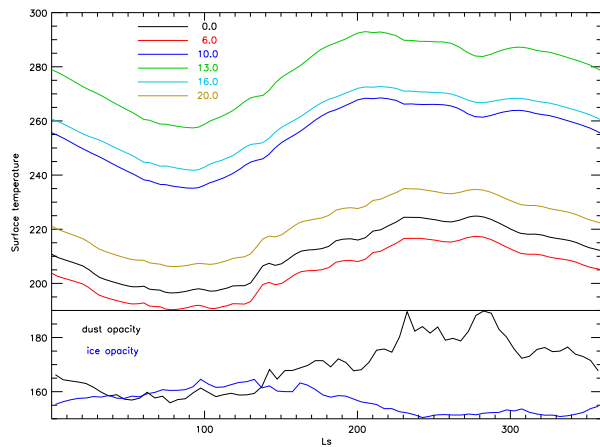


**Figure 12.** Seasonal variation of surface temperatures (upper section of figure) at the nominal MSL landing site on the floor of Gale crater. A horizon elevated  $3.5^\circ$  in all directions was used.  $A = 0.215$ ,  $I = 313$ , elev =  $-4440$ ,  $\epsilon = 0.97$ . Temperatures are shown for 6 h spacing through the night and for the warmest time of day and 3 h to either side; indicated by the upper legend. The lower section shows the infrared opacity of dust and ice from the TES climate model interpolated to  $4.5^\circ\text{S}$ , both at the same scale, the maximum for dust is 0.398 for the climate model standard 610 Pa surface pressure. The TES climate is linearly interpolated to the KRC seasons, so the climate perturbations to the smooth seasonal variation do not have exactly the same shape as the opacity data.

[174] KRC was run using 18 latitudes in each hemisphere from  $45^\circ$  to near the pole, with zonal-average elevations, 80 seasons with a 3 year spin-up. The atmospheric dust and ice opacity followed the annual variation measured by THEMIS, averaged over about 5 Mars years (digital data from M. Smith [Smith, 2009]). The frost emissivity was 0.95; other surface and frost parameters are close to the observed average values (see Figure 13 caption). By combining the seasonal frost budgets for the south and north hemispheres from different KRC runs (each with globally uniform properties), KRC seasonal frost models can approximate the Viking pressure curves [Tillman *et al.*, 1993], adjusted to the mean surface elevation of Mars, see Figure 13. These runs indicate that the total inventory of gas participating in the seasonal cycle is equivalent to a mean annual pressure at the mean surface level of about 741 Pa; Wood and Paige [1992] obtained 771 to 798 Pa in their best fits.

[175] Use of uniform thermal inertia and frost albedo relations across each seasonal cap is a significant oversimplification for Mars; yet the basic features are captured by the KRC model. The time around  $L_s = 330^\circ$  is not well matched, probably due to the great variation of solid  $\text{CO}_2$  albedo in the southern spring [Kieffer *et al.*, 2000; Colaprete *et al.*, 2005; Glenar *et al.*, 2005; Brown *et al.*, 2010]. Nonetheless, KRC can be used to quickly estimate the differential effect of changing cap-related parameters.

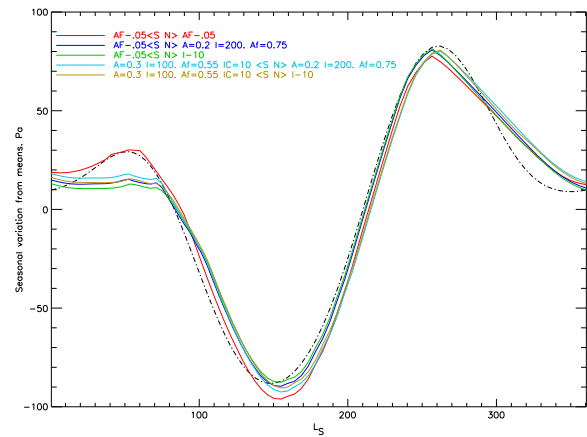


**Figure 13.**  $\text{CO}_2$  frost budget expressed as changes of surface pressure at the mean surface elevation of Mars ( $-0.55$  km). The base model was: South:  $A = 0.3$ ,  $I = 100$ ,  $A_f = 0.55$ ,  $IC = 10$  (6 cm), North:  $A = 0.2$ ,  $I = 200$ ,  $A_f = 0.75$ ,  $IC = 10$  (12 cm);  $A$  is the ground albedo,  $I$  is the ground thermal inertia,  $A_f$  is the albedo of thick frost,  $IC$  is the first layer with lower-material (ice) properties. Other annotations in the legend indicate changes from the base models listing, top down, the best fitting set of models (in terms of mean absolute residual) in the set of 16 hemisphere combinations of four models in each hemisphere consisting of the base, and three separate offsets:  $A_f - 0.05$ ,  $I - 10$ , and  $IC - 2$  (3.6 and 7.2 cm). See text for other model parameters. The dot-dashed line shows the average pressure variation observed by Viking.

## 7. Summary

[176] KRC provides an efficient and effective way to compute planetary surface temperature and top-of-atmosphere bolometric temperatures useful for remote sensing. Its physics-based one-layer gray atmosphere provides a reasonable approximation of the radiative effects of a dusty atmosphere; it does not incorporate any effect of winds. Advantages include its wide use, versatility, rapid execution, and multiple binary output formats. It has evolved over five decades and been used in a large number of analyses of thermal infrared observations. The program runs in FORTRAN with some C utility routines; a variety of IDL routines are available to read the output files.

[177] For Mars, the values shown in the sample input file should be adequate for most studies. Temperature-dependent conductivity and specific heat can be included, but would not be needed unless differences on the order of 1 K are important. The ability to handle slopes of any direction and realistic magnitude can be used wherever topography is important; the ability to consider elevated horizons to first order is useful for crater interiors. The one-point mode provides a simple interface for multiple specific conditions (outside the seasonal cap). The rapid execution makes it practical to use multiple year spin-up, which ameliorates any biases of starting conditions. It will accept a climate model of atmosphere dust and ice opacity versus season and latitude. The code, documentation, and sample files, as well as the ability to construct input cases and run a precompiled KRC, are intended to be permanently available to anyone at <http://krc.mars.asu.edu>.

[178] **Acknowledgments.** Funding for development of KRC was provided by NASA. Funding for this manuscript provided by NASA THEMIS contract 1228404 through Arizona State University. Presubmission reviews by Phil Christensen, Robin Fergason, and Sylvain Piqueux were a great help. Formal reviews by Mikhail Kreslavsky and an anonymous reviewer were challenging and much appreciated.

## References

- Aharonson, O., and N. Schorghofer (2006), Subsurface ice on Mars with rough topography, *J. Geophys. Res.*, **111**(E10), 11,007–+, doi:10.1029/2005JE002636.
- Allison, M., and M. McEwen (2000), A post-Pathfinder evaluation of areo-centric solar coordinates with improved timing recipes for Mars seasonal/diurnal climate studies, *Planet Space Sci.*, **48**, 215–235, doi:10.1016/S0032-0633(99)00092-6.
- Arvidson, R., et al. (2008), Mars Exploration Program 2007 Phoenix landing site selection and characteristics, *J. Geophys. Res.*, **113**(E12), 0–+, doi:10.1029/2007JE003021.
- Arvidson, R. E., et al. (2004), Localization and Physical Properties Experiments Conducted by Spirit at Gusev Crater, *Science*, **305**, 821–824, doi:10.1126/science.1109922.
- Arvidson, R. E., et al. (2006), Nature and origin of the hematite-bearing plains of Terra Meridiani based on analyses of orbital and Mars Exploration rover data sets, *J. Geophys. Res.*, **111**(E10), 12–+, doi:10.1029/2006JE002728.
- Aumann, H. H., and H. H. Kieffer (1973), Determination of particle sizes in Saturn's rings from their eclipse cooling and heating curves, *Astron. J.*, **183**, 305–311.
- Balme, M., N. Mangold, D. Baratoux, F. Costard, M. Gosselin, P. Masson, P. Pinet, and G. Neukum (2006), Orientation and distribution of recent gullies in the southern hemisphere of Mars: Observations from High Resolution Stereo Camera/Mars Express (HRSC/MEX) and Mars Orbiter Camera/Mars Global Surveyor (MOC/MGS) data, *J. Geophys. Res.*, **111**(E10), E05001, doi:10.1029/2005JE002607.
- Bandfield, J. L. (2007), High-resolution subsurface water-ice distributions on Mars, *Nature*, **447**, 64–67, doi:10.1038/nature05781.
- Bandfield, J. L., and C. S. Edwards (2008), Derivation of martian surface slope characteristics from directional thermal infrared radiometry, *Icarus*, **193**, 139–157, doi:10.1016/j.icarus.2007.08.028.
- Bandfield, J. L., and W. C. Feldman (2008), Martian high latitude permafrost depth and surface cover thermal inertia distributions, *J. Geophys. Res.*, **113**(E12), 8001–+, doi:10.1029/2007JE003007.
- Barnes, J. R., J. B. Pollack, R. M. Haberle, C. B. Leovy, R. W. Zurek, H. Lee, and J. Schaeffer (1993), Mars atmospheric dynamics as simulated by the NASA AMES General Circulation Model. II - Transient baroclinic eddies, *J. Geophys. Res.*, **98**, 3125–3148.
- Basu, S., M. I. Richardson, and R. J. Wilson (2004), Simulation of the Martian dust cycle with the GFDL Mars GCM, *J. Geophys. Res.*, **109**(E18), 11,006–+, doi:10.1029/2004JE002243.
- Bell, J. (2008), *The Martian Surface: Composition, Mineralogy, and Physical Properties*, chap. 9, 635 pp., Cambridge Univ. Press, Cambridge, U. K.
- Berman, R. G., and T. H. Brown (1985), Heat capacity of minerals in the system  $\text{Na}_2\text{O}-\text{K}_2\text{O}-\text{CaO}-\text{MgO}-\text{FeO}-\text{Fe}_2\text{O}_3-\text{Al}_2\text{O}_3-\text{SiO}_2-\text{TiO}_2-\text{H}_2\text{O}-\text{CO}_2$ : representation, estimation, and high temperature extrapolation, *Contrib. Mineral. Petrol.*, **89**, 168–183, doi:10.1007/BF00379451.
- Bertoldi, C., E. Dachs, and P. Appel (2007), Heat-pulse calorimetry measurements on natural chlorite-group minerals, *Am. Mineral.*, **92**, 553–559.
- Birch, F., and H. Clark (1940), Thermal conductivity of rocks and its dependence upon temperature and composition, *Am. J. Sci.*, **238**, 529–558.
- Brown, A. J., W. M. Calvin, P. C. McGuire, and S. L. Murchie (2010), Compact Reconnaissance Imaging Spectrometer for Mars (CRISM) south polar mapping: First Mars year of observations, *J. Geophys. Res.*, **115**(E14), E00D13, doi:10.1029/2009JE003333.
- Cahill, D. G., S. K. Watson, and R. O. Pohl (1992), Lower limit to the thermal conductivity of disordered crystals, *Phys. Rev. B*, **46**(10), 6131–6140, doi:10.1103/PhysRevB.46.6131.
- Carslaw, H. S., and J. C. Jaeger (1959), *Conduction of heat in solids*, Oxford Univ. Press, London, 2nd ed., 510 pp.
- Christensen, P. R. (1986), The spatial distribution of rocks on Mars, *Icarus*, **68**, 217–238, doi:10.1016/0019-1035(86)90020-5.
- Christensen, P. R., et al. (2003), Morphology and composition of the surface of Mars: Mars Odyssey THEMIS results, *Science*, **300**, 2056–2061.
- Christensen, P. R., et al. (2004), Initial Results from the Mini-TES Experiment in Gusev Crater from the Spirit Rover, *Science*, **305**, 837–842, doi:10.1126/science.1100564.
- Christensen, P. R., et al. (2005a), Mars Exploration Rover candidate landing sites as viewed by THEMIS, *Icarus*, **176**, 12–43, doi:10.1016/j.icarus.2005.01.004.
- Christensen, P. R., et al. (2005b), Evidence for magmatic evolution and diversity on Mars from infrared observations, *Nature*, **436**, 504–509, doi:10.1038/nature03639.
- Clancy, R. T., M. J. Wolff, and P. R. Christensen (2003), Mars aerosol studies with the MGS TES emission phase function observations: Optical depths, particle sizes, and ice cloud types versus latitude and solar longitude, *J. Geophys. Res.*, **108**(E9), 2–1.
- Clauser, C., and E. Huenges (1995), Thermal conductivity of rocks and minerals, in *Rock Physics and Phase Relations: a Handbook of Physical Constants*, edited by T. J. Ahrens, pp. 105–126, AGU, Washington, D.C.
- Clifford, S. M., and C. J. Bartels (1986), The Mars Thermal Model (marstherm): a FORTRAN 77 Finite-Difference Program Designed for General Distribution, in *Lunar and Planetary Institute Conference Abstracts*, pp. 142–143, Houston, Tex.
- Colaprete, A., J. R. Barnes, R. M. Haberle, J. L. Hollingsworth, H. H. Kieffer, and T. N. Titus (2005), Albedo of the south pole on Mars determined by topographic forcing of atmosphere dynamics, *Nature*, **435**, 184–188, doi:10.1038/nature03561.
- Debye, P. (1912), Zur theorie der spezifischen wärmen, *Ann. Phys.*, **344**, 789–839, (Translation in *The Collected papers of Peter J. W. Debye*, Interscience, New York, 1954.).
- DiTeon, R. (1982), Daily temperature variations on Mars, *J. Geophys. Res.*, **87**, 10,197–10,214.
- Edgett, K. S., and P. R. Christensen (1991), The particle size of Martian aeolian dunes, *J. Geophys. Res.*, **96**, 22,765–+.
- Ezell, E., and L. Ezell (1984), *On Mars, Exploration of the red planet, 1958–1978*, SP, vol. 4212, NASA, Washington D.C..
- Feldman, W. C., M. C. Bourke, R. C. Elphic, S. Maurice, J. Bandfield, T. H. Prettyman, B. Diez, and D. J. Lawrence (2008), Hydrogen content of sand dunes within Olympia Undae, *Icarus*, **196**, 422–432, doi:10.1016/j.icarus.2007.08.044.
- Fergason, R. L., P. R. Christensen, J. F. Bell, M. P. Golombek, K. E. Herkenhoff, and H. H. Kieffer (2006a), Physical properties of the Mars Exploration Rover landing sites as inferred from Mini-TES-derived thermal inertia, *J. Geophys. Res.*, **111**(E10), 2–+, doi:10.1029/2005JE002583.
- Fergason, R. L., P. R. Christensen, and H. H. Kieffer (2006b), High resolution thermal inertia derived from THEMIS: thermal model and applications, *J. Geophys. Res.*, **111**, E12,004, doi:10.1029/2006JE002735.

- Ferguson, R. L., P. R. Christensen, M. Golombek, and T. Parker (2012), Surface properties of the Mars Science Laboratory Candidate Landing Sites: Characterization from Orbit and Predictions, *Space Sci. Rev.*, **170**, 739–773, doi:10.1007/s11214-012-9891-3.
- Forget, F., F. Hourdin, and O. Talagrand (1998), CO<sub>2</sub> snowfall on Mars: Simulation with a general circulation model, *Icarus*, **131**, 302–316.
- Gatley, I., H. H. Kieffer, E. Miner, and G. Neugebauer (1974), Infrared observations of Phobos from Mariner 9, *Astrophys. J.*, **190**, 497–503.
- Glenar, D. A., G. Hansen, G. Bjoraker, M. Smith, J. Pearl, and D. Blaney (2005), Bright-region radiative properties within the Mars south polar cap ( $L_s=231$ ) from near-infrared spectroscopic imaging, *Icarus*, **174**, 600–603, doi:10.1016/j.icarus.2004.09.012.
- Glotch, T. D., and P. R. Christensen (2005), Geologic and mineralogic mapping of Aram Chaos: Evidence for a water-rich history, *J. Geophys. Res.*, **110**(E9), 9006–+, doi:10.1029/2004JE002389.
- Golombek, M. P., R. A. Cook, H. J. Moore, and T. J. Parker (1997a), Selection of the Mars Pathfinder landing site, *J. Geophys. Res.*, **102**, 3967–3988, doi:10.1029/96JE03318.
- Golombek, M. P., et al. (1997b), Overview of the Mars Pathfinder Mission and Assessment of Landing Site Predictions, *Science*, **278**, 1743–+.
- Golombek, M. P., et al. (2003), Selection of the Mars Exploration Rover landing sites, *J. Geophys. Res.*, **108**, 8072–+, doi:10.1029/2003JE002074.
- Golombek, M. P., et al. (2005), Assessment of Mars Exploration Rover landing site predictions, *Nature*, **436**, 44–48, doi:10.1038/nature03600.
- Golombek, M. P., et al. (2006), Geology of the Gusev cratered plains from the Spirit rover transverse, *J. Geophys. Res.*, **111**(E10), 2–+, doi:10.1029/2005JE002503.
- Golombek, M. P., et al. (2012), Selection of the Mars Science Laboratory Landing Site, *Space Sci. Rev.*, **170**, 641–737, doi:10.1007/s11214-012-9916-y.
- Greeley, R., et al. (2006), Gusev crater: Wind-related features and processes observed by the Mars Exploration Rover Spirit, *J. Geophys. Res.*, **111**(E10), 2–+, doi:10.1029/2005JE002491.
- Haberle, R. M., and B. M. Jakosky (1991), Atmospheric effects on the remote determination of thermal inertia on Mars, *Icarus*, **90**, 187–204.
- Haberle, R. M., J. B. Pollack, J. R. Barnes, R. W. Zurek, C. B. Leovy, J. R. Murphy, H. Lee, and J. Schaeffer (1993), Mars atmospheric dynamics as simulated by the NASA AMES General Circulation Model. I - The zonal-mean circulation, *J. Geophys. Res.*, **98**, 3093–3123.
- Haberle, R. M., F. Forget, A. Colaprete, J. Schaeffer, W. V. Boynton, N. J. Kelly, and M. A. Chamberlain (2008), The effect of ground ice on the Martian seasonal CO<sub>2</sub> cycle, *Planet. Space Sci.*, **56**, 251–255, doi:10.1016/j.pss.2007.08.006.
- Helbert, J., J. Benkhoff (2003), A new approach to assessing the burial depth of ground ice deposits and its application to proposed MER landing sites in Isidis Planitia, *J. Geophys. Res.*, **108**, 8087, October 2003.
- Hobbs, P. V. (1974), *Ice Physics*, 830 pp., Oxford Univ. Press, London, U. K.
- Horai, K., and G. Simmons (1970), An empirical relationship between thermal conductivity and Debye temperature for silicates, *J. Geophys. Res.*, **75**, 978–982, doi:10.1029/JB075i005p00978.
- Horai, K., and S. Simmons (1969), Thermal conductivity of rock-forming minerals, *Earth Planet. Sci. Lett.*, **6**, 359–368.
- Hourdin, F., F. Forget, and O. Talagrand (1995), The sensitivity of the Martian surface pressure and atmospheric mass budget to various parameters: A comparison between numerical simulations and Viking observations, *J. Geophys. Res.*, **100**, 5501–5523, doi:10.1029/94JE03079.
- Jakosky, B. M., M. T. Mellon, H. H. Kieffer, P. R. Christensen, E. S. Varnes, and S. W. Lee (2000), The thermal inertia of Mars from the Mars Global Surveyor Thermal Emission Spectrometer, *J. Geophys. Res.*, **105**, 9643–9652.
- James, P. B., H. H. Kieffer, and D. A. Paige (1992), The seasonal cycle of carbon dioxide on Mars, in *Mars*, edited by H. H. Kieffer et al., chap. 27, pp. 934–968, Univ. of Ariz. Press, Tucson.
- Joseph, J. H., W. J. Wiscombe, and J. A. Weinman (1976), The delta-Eddington approximation for radiative flux transfer, *J. Atmos. Sci.*, **33**, 2452–2459.
- Kieffer, H. H. (2007), Cold jets in the Martian polar caps, *J. Geophys. Res.*, **112**(E11), 8005–+, doi:10.1029/2006JE002816.
- Kieffer, H. H. (2009), Particulate thermal conduction, TES/THEMIS Team internal memo, LaTeX document.
- Kieffer, H. H. (2010), Temperature dependence of rock thermal properties, TES/THEMIS Team internal memo, LaTeX document.
- Kieffer, H. H., T. Z. Martin, A. R. Peterfreund, B. M. Jakosky, E. D. Miner, and F. D. Palluconi (1977), Thermal and albedo mapping of Mars during the Viking primary mission, *J. Geophys. Res.*, **82**, 4249–4291.
- Kieffer, H. H., B. M. Jakosky, C. W. Snyder, and E. M. S. Matthews (1992), *Mars*, University of Arizona Press, Tucson, 1498 pp.
- Kieffer, H. H., T. N. Titus, K. F. Mullins, and P. Christensen (2000), Mars south polar spring and summer behavior observed by TES: Seasonal cap evolution controlled by frost grain size, *J. Geophys. Res.*, **105**(E4), 9653–9699.
- Kieffer, S. W. (1979), Thermodynamics and lattice vibrations of minerals. I - Mineral heat capacities and their relationships to simple lattice vibrational models. II - Vibrational characteristics of silicates. III - Lattice dynamics and an approximation for minerals with application to simple substances and framework silicates, *Rev. Geophys. Space Phys.*, **17**, 1–59.
- Kittel, C. (1976), *Introduction to Solid State Physics*, 5th Ed, 599 pp., Wiley, New York.
- Ledlow, M. J., M. Zeilik, J. O. Burns, G. R. Gisler, J. Zhao, and D. N. Baker (1992), Subsurface emissions from Mercury - VLA radio observations at 2 and 6 centimeters, *Astrophys. J.*, **384**, 640–655, doi:10.1086/170906.
- Lunine, J. I., G. Neugebauer, and B. M. Jakosky (1982), Infrared observations of PHOBOS and Deimos from Viking, *J. Geophys. Res.*, **87**, 10,297–10,305, doi:10.1029/JB087iB12p10297.
- Malin, M. C., and K. S. Edgett (2000), Evidence for recent ground water seepage and surface runoff on Mars, *Science*, **288**, 2330–2335.
- Malin, M. C., K. S. Edgett, L. V. Posiolova, S. M. McColley, and E. Z. N. Dobra (2006), Present-Day Impact Cratering Rate and Contemporary Gully Activity on Mars, *Science*, **314**, 1573–, doi:10.1126/science.1135156.
- Mangold, N., A. Mangeney, V. Migeon, V. Ansan, A. Lucas, D. Baratoux, and F. Bouchut (2010), Sinuous gullies on Mars: Frequency, distribution, and implications for flow properties, *J. Geophys. Res.*, **115**(E14), E11001, doi:10.1029/2009JE003540.
- Martin, T. Z. (1986), Thermal infrared opacity of the Mars atmosphere, *Icarus*, **66**, 2–21, doi:10.1016/0019-1035(86)90003-5.
- Martin, T. Z. (2004), Thermal correction of MRO CRISM data using photolithometry and slope-dependent thermal models for the Martian surface, *Bulletin of the American Astronomical Society*, **36**, 1160–+.
- Mellon, M. T., B. M. Jakosky, H. H. Kieffer, and P. R. Christensen (2000), High-resolution thermal inertia mapping from the Mars Global Surveyor Thermal Emission Spectrometer, *Icarus*, **148**, 437–455.
- Nowicki, S. A., and P. R. Christensen (2007), Rock abundance on Mars from the Thermal Emission Spectrometer, *J. Geophys. Res.*, **112**(E11), 5007–+, doi:10.1029/2006JE002798.
- Osterloo, M., V. Hamilton, J. Bandfield, T. Glotch, A. Baldrige, P. Christensen, L. Tornabene, and F. Anderson (2008), Chloride-bearing materials in the Southern highlands of Mars, *Science*, **319**, 1651.
- Paige, D. A. (1985), The annual heat balance of the Martian polar caps from Viking observations, Ph.D. thesis, California Inst. of Technology.
- Paige, D. A. (1992), The thermal stability of near-surface ground ice on Mars, *Nature*, **356**, 43–45.
- Paige, D. A., and K. D. Keegan (1994), Thermal and albedo mapping of the polar regions of Mars using Viking thermal mapper observations 2. south polar region, *J. Geophys. Res.*, **99**, 25,993–26,013.
- Paige, D. A., and S. E. Wood (1992), Modeling the Martian Seasonal CO<sub>2</sub> Cycle. 2. Interannual variability, *Icarus*, **99**, 15–27.
- Paige, D. A., J. E. Bachman, and K. D. Keegan (1994), Thermal and albedo mapping of the polar regions of Mars using Viking thermal mapper observations 1. north polar region, *J. Geophys. Res.*, **99**, 25,959–25,991.
- Petrin, G., and V. Popov (1995), Temperature dependence of lattice thermal conductivity of earths mineral substance, *Phys. Solid Earth*, **30**, 617–623.
- Phillips, R. J., et al. (2008), Mars North Polar Deposits: Stratigraphy, Age, and Geodynamical Response, *Science*, **320**, 1182–, doi:10.1126/science.1157546.
- Piqueux, S., and P. Christensen (2008), North and south subice gas flow and venting of the seasonal caps of Mars: A major geomorphological agent, *J. Geophys. Res.*, **113**, E06005, doi:10.1029/2007JE003009.
- Piqueux, S., and P. Christensen (2009a), A model of thermal conductivity in planetary soils: 1. Theory for unconsolidated soils, *J. Geophys. Res.*, **114**(E13), 9005–+, doi:10.1029/2008JE003308.
- Piqueux, S., and P. Christensen (2009b), A model of thermal conductivity in planetary soils: 2. Theory for cemented soils, *J. Geophys. Res.*, **114**(E13), 9006–+, doi:10.1029/2008JE003309.
- Piqueux, S., C. Edwards, and P. Christensen (2008), Distribution of the ices exposed near the south pole of Mars using Thermal Emission Imaging System (THEMIS) temperature measurements, *J. Geophys. Res.*, **113**, E08014, doi:10.1029/2007JE003035.
- Presley, M. A., and P. R. Christensen (1997), Thermal conductivity measurements of particulate materials 2. Results, *J. Geophys. Res.*, **102**(E3), 6551–6566.
- Putzig, N. E., and M. T. Mellon (2007), Apparent thermal inertia and the surface heterogeneity of Mars, *Icarus*, **191**, 68–94, doi:10.1016/j.icarus.2007.05.013.
- Putzig, N. E., M. T. Mellon, K. A. Kretke, and R. E. Arvidson (2005), Global thermal inertia and surface properties of Mars from the MGS mapping mission, *Icarus*, **173**, 325–341, doi:10.1016/j.icarus.2004.08.017.
- Reiss, D., S. van Gasselt, G. Neukum, and R. Jaumann (2004), Absolute dune ages and implications for the time of formation of gullies in Nirgal Vallis, Mars, *J. Geophys. Res.*, **109**(E18), E06007, doi:10.1029/2004JE002251.
- Richardson, M. I., R. J. Wilson, and A. V. Rodin (2002), Water ice clouds in the Martian atmosphere: General circulation model experiments with a



- simple cloud scheme, *J. Geophys. Res.*, **107**, 5064–+, doi:10.1029/2001JE001804.
- Rogers, A. D., P. R. Christensen, and J. L. Bandfield (2005), Compositional heterogeneity of the ancient Martian crust: Analysis of Ares Vallis bedrock with THEMIS and TES data, *J. Geophys. Res.*, **110**(E9), 5010–+, doi:10.1029/2005JE002399.
- Ruff, S. W., et al. (2001), Mars' "White Rock" feature lacks evidence of an aqueous origin: Results from Mars Global Surveyor, *Jour. Geophys. Res.*, **106**(15), 23,921–23,928.
- Ruiz, J., V. López, and J. M. Dohm (2010), The present-day thermal state of Mars, *Icarus*, **207**, 631–637, doi:10.1016/j.icarus.2010.01.016.
- Sass, J., C. Stone, and R. Munroe (1984), Thermal conductivity determinations on solid rock: a comparison between a steady-state divided-bar apparatus and a commercial transient line-source device, *J. Volcanol. Geotherm. Res.*, **20**, 145–153.
- Sass, J. H., A. H. Lachenbruch, T. H. Moses, Jr., and P. Morgan (1992), Heat flow from a scientific research well at Cajon Pass, California, *J. Geophys. Res.*, **97**, 5017–5030, doi:10.1029/91JB01504.
- Schorghofer, N. (2008), Temperature response of Mars to Milankovitch cycles, *Geophys. Res. Lett.*, **35**, L18201, doi:10.1029/2008GL034954.
- Schorghofer, N., and O. Aharonson (2005), Stability and exchange of subsurface ice on Mars, *J. Geophys. Res.*, **110**(E9), 5003–+, doi:10.1029/2004JE002350.
- Seidelmann, K. P. (Ed.) (2005), *Explanatory Supplement to the Astronomical Almanac*, University Science Books, Mill Valley, California.
- Seidelmann, P. K., L. E. Doggett, and M. R. Deluccia (1974), Mean elements of the principal planets, *Astron. J.*, **79**, 57–+.
- Seidelmann, P. K., et al. (2005), Report of the IAU/IAG Working Group on Cartographic Coordinates and Rotational Elements: 2003, *Celestial Mechanics and Dynamical Astronomy*, **91**, 203–215, doi:10.1007/s10569-004-3115-4.
- Seipold, U., and E. Huenges (1998), Thermal properties of gneisses and amphibolites: high pressure and high temperature investigations of ktb-rock samples, *Tectonophysics*, **291**, 173–178.
- Shettle, E. P., and J. A. Weinman (1970), The Transfer of Solar Irradiance Through Inhomogeneous Turbid Atmospheres Evaluated by Eddington's Approximation, *J. Atmos. Sci.*, **27**, 1048–1055.
- Smith, M. D. (2004), Interannual variability in TES atmospheric observations of Mars during 1999–2003, *Icarus*, **167**, 148–165, doi:10.1016/S0019-1035(03)00287-2.
- Smith, M. D. (2009), THEMIS observations of Mars aerosol depth from 2002–2008, *Icarus*, **202**, 444–452.
- Tillman, J. E., N. C. Johnson, P. Gettorp, and D. B. Percival (1993), The Martian annual atmospheric pressure cycle: years without great dust storms, *J. Geophys. Res.*, **98**, 10,963–10,971.
- Titus, T. N., H. H. Kieffer, and K. F. Mullins (2001), Slab ice and snow flurries in the Martian polar night, *J. Geophys. Res.*, **106**(E10), 23,181–23,196.
- Titus, T. N., H. H. Kieffer, and P. N. Christensen (2003), Exposed water ice discovered near the south pole of Mars, *Science*, **299**, 1048–1051.
- Vasavada, A. R., D. A. Paige, and S. E. Wood (1999), Near-Surface Temperatures on Mercury and the Moon and the Stability of Polar Ice Deposits, *Icarus*, **141**, 179–193, doi:10.1006/icar.1999.6175.
- Vosteen, H., and R. Schellschmidt (2003), Influence of temperature on thermal conductivity, thermal capacity and thermal diffusivity of different rock types, *Phys. Chem. Earth*, **28**, 499–509.
- Waples, D., and J. Waples (2004), A review and evaluation evaluation of specific heat capacities of rocks, minerals, and subsurface fluids. part 1: Minerals and nonporous rocks, *Natural Resources Res.*, **13**, 97–112.
- Wechsler, A. E., and P. E. Glaser (1965), Pressure Effects on Postulated Lunar Materials, *Icarus*, **4**, 335–+, doi:10.1016/0019-1035(65)90038-2.
- Weissman, P. R., and H. H. Kieffer (1981), Thermal modeling of cometary nuclei, *Icarus*, **47**, 302–311.
- Wilson, R. J., and K. Hamilton (1996), Comprehensive model simulation of thermal tides in the Martian atmosphere, *J. Atmos. Sci.*, **53**, 1290–1326, doi:10.1175/1520-0469(1996)053.
- Wood, S. E., and D. A. Paige (1992), Modeling the Martian seasonal CO<sub>2</sub> cycle; 1. Fitting the Viking Lander pressure curves, *Icarus*, **99**, 1–14.
- Zoth, G., and R. Haenel (1988), Appendix, in *Handbook of Terrestrial Heat-Flow Density Determination*, edited by R. Haenel, L. Rybach, and L. Stegena, pp. 449–468, Kluwer Acad. Publishers, Dordrecht.
- Zuber, M. T., et al. (2000), Internal Structure and Early Thermal Evolution of Mars from Mars Global Surveyor Topography and Gravity, *Science*, **287**, 1788–1793, doi:10.1126/science.287.5459.1788.